

学位論文

**Study on Single-molecular Rotors, Copper-Pyrimidine Complexes:
Electroanalysis and STM Observation of Redox-synchronized Ring Rotation**

(銅-ピリミジン錯体単分子ローターの研究:
レドックスに連動した環回転の電気化学解析と STM 観察)

平成 26 年 12 月博士 (理学) 申請

東京大学大学院理学系研究科化学専攻

高良 祐亮

Abstract

After the decades of molecular machines works focusing on the construction of a molecule-based system for the realization of molecular electronic devices, the main issue is now moving on to the development of methods to access single molecules. I employed the copper-pyrimidine complexes and visualized its rotational behavior as the changes of the electronic density distribution at single-molecule level by scanning tunneling microscopy (STM).

In chapter 1, important area of background data and the focus and the concept of this thesis are described.

In chapter 2, the rotational behavior of copper-pyrimidine complexes immobilized on gold electrodes is elucidated by cyclic voltammetry. The rotational motion of the copper complexes immobilized on gold could be controlled by an applied electric potential from the electrodes. A quantitative analysis on cyclic voltammograms revealed that the rotation rate on the electrode decreased to about one-tenth of that in the solution state, allowing the observation of rotational motion with STM.

In chapter 3, the rotational isomerization visualized at the single-molecule level is discussed. STM observation was conducted on the mixed-SAMs consisting of hexanethiol and copper complex molecules. The copper complexes inserted into hexanethiol SAM were successfully visualized. In successive scan, the complex molecules showed conductivity changes between the two states, assigned to the two isomers in terms of their electronic states.

In chapter 4, a twin rotor, copper-bipyrimidine complex, was studied. The aim of this research is to achieve tristability with the rotational isomerization of this system. $^1\text{H-NMR}$ and cyclic voltammetry revealed that three isomers coexist and the electrochemical potential change of the twin rotor was more than twice of that of a single rotor. Furthermore, the clear difference between each rotational step was turned out by variable-temperature $^1\text{H-NMR}$ experiment and simulative analysis, suggesting a correlation between the two rotors.

In chapter 5, the concluding remarks are given.

Contents

Abstract

Chapter 1 General introduction	1
1-1 Molecular device	2
1-2 Single molecule study by scanning probe microscopy	2
1-3 Application of SPM to molecular device works	4
1-4 Challenges for molecular device by SPM	6
1-5 Molecular motion in transition metal complexes	6
1-6 Cu-pyrimidine system	8
1-7 Aim of this research	9
1-8 References	10
Chapter 2 Electrochemical Analysis of Cu-pyrimidine Complexes Immobilized on Au Surface	15
2-1 Introduction	16
2-2 Experimental	17
2-2-1 Materials	17
2-2-2 Synthesis	17
2-2-3 Experimental apparatus	23
2-3 Results and discussion	25
2-3-1 X-ray structural analysis	25
2-3-2 ¹ H-NMR measurements in solution state	29
2-3-3 Cyclic voltammetry in solution state	32
2-3-4 XPS measurements on electrode surface	34
2-3-5 Cyclic voltammetry on electrode surface	35
2-3-6 Simulative analysis on rotational behavior	38
2-3-7 Thermodynamics and kinetics of rotation on Au surface	44
2-3-8 Repeatability of redox-synchronized rotation	46
2-4 Conclusion	47
2-5 References	48

Chapter 3 STM Observation of Rotational Motion	49
3-1 Introduction	50
3-2 Experimental	51
3-2-1 Materials	51
3-2-2 Synthesis	51
3-2-3 Experimental apparatus	54
3-3 Results and Discussion	55
3-3-1 Control of surface density	55
3-3-2 STM observation under ambient condition	57
3-3-3 Origin of blinking behavior	61
3-3-4 Comparison with Cu-bipyridine complex	64
3-3-5 STM observation under UHV condition	66
3-4 Conclusion	67
3-5 References	68
Chapter 4 Two-Step Rotation of a Twin Rotor	69
4-1 Introduction	70
4-2 Experimental	72
4-2-1 Materials	72
4-2-2 Synthesis	73
4-2-3 Experimental apparatus	74
4-3 Results and discussion	75
4-3-1 Variable-temperature ¹ H NMR	75
4-3-2 Cyclic voltammetry	81
4-3-3 Kinetic and thermodynamic properties of two rotational steps	86
4-4 Conclusion	89
4-5 References	90
Chapter 5 Concluding Remarks	91
Publication	95
Acknowledgement	97

Chapter 1

General Introduction

1-1 Molecular device

The concept of an electronic device consisting of molecules, which was first proposed by A. Aviram and M. A. Ratner,¹ has excited researchers' curiosities to make a research field for molecular devices.² Their motivation is based on the possibility to replace silicon-based devices by the unique functionalities of molecules; for example, the capability of tuning properties by synthetic methodology and the responsiveness to various kinds of stimuli including optical,^{3,4} magnetic,^{5,6} electric,⁷⁻⁹ chemical¹⁰ and mechanical signals.^{11,12}

Since conventional electric devices work in the solid state, behavior in the solid state is an initial requirement for molecular devices, consequently, self-assembly of molecules on electrode surfaces has been one promising approach not only to fulfill the necessity, but also to ensure the validity of molecular device research owing to the dense packing of molecular units on the surface, which can lead to miniaturization of devices.¹³

1-2 Single molecule study by scanning probe microscopy

The development of the components for molecule-based systems was well established in the field of chemistry. On the other hand, in the field of physics, microscopic technique has matured to visualize single molecules, which is described in this section.

Since G. Binnig and H. Rohrer reported the atomic resolution image of 7×7 reconstruction on Si(111) by using scanning tunneling microscopy (STM),¹⁴ their concept has spread over the world and made a research field of scanning probe microscopy, which is abbreviated as SPM. The high resolution of STM is accomplished by bringing an atomically sharp metal tip close to a conductive surface. When a bias voltage is applied between the probe tip and surface, electrons are allowed to tunnel quantum mechanically between them and current flows for so-called "tunneling effect." For its operating principle, STM is extremely sensitive to surface electronic state, and thus it is capable of visualizing the local density of states of surface. Consequently, STM has been fully utilized for the precise understanding of the electronic states of molecules, especially focusing on π -conjugated and planar molecules.

Figure 1-1 shows one example that succeeded in resolving the electronic state of pentacene adsorbed on NaCl layer on Cu(111). NaCl was used as an insulator to

decouple the electronic states of the molecules from that of the Cu surface. The experimental images (Fig. 1-1 a, b) share characteristics with the calculated ones (Fig. 1-1 g, h). Of particular note for this paper is that the authors functionalized an STM tip with a CO molecule, which resulted in an enhanced lateral resolution due to the $2\pi^*$ orbitals of CO. Such a capability of functionalizing tips had also made this method even more promising in single molecular study.

Some quantum mechanical properties, such as giant magnetoresistance,¹⁵ Kondo effects¹⁶ and quantum interference,¹⁷ have also been found at single-molecule levels by means of SPM.

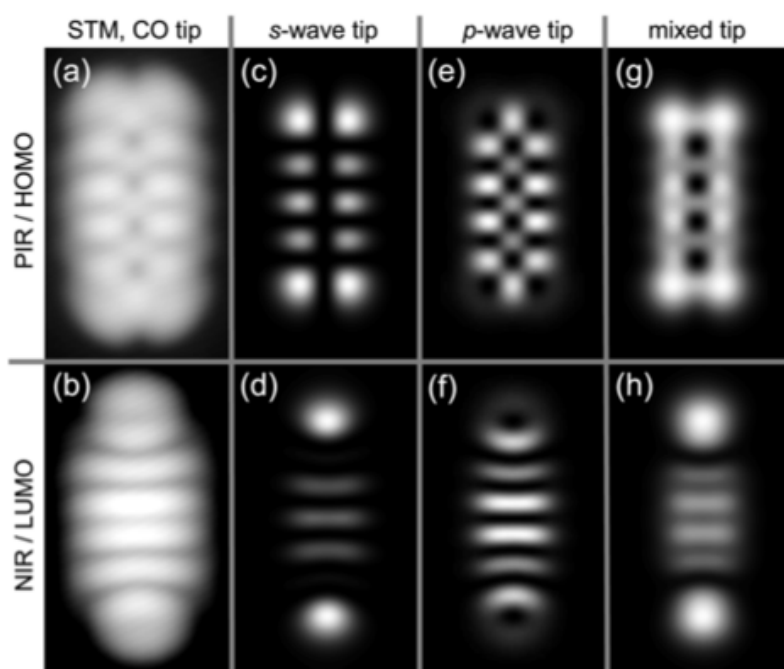


Fig. 1-1 STM measurements of pentacene on NaCl(2 ML) on Cu(111) using a CO tip at the onset (a) of the PIR at $V = -2.15\text{V}$, $I = 0.9\text{ pA}$, and (b) of the NIR at $V = 1.25\text{V}$, $I = 1.3\text{ pA}$. Calculated STM images at $z_0 = 4.5\text{ \AA}$ of the HOMO and LUMO of the isolated molecule, respectively, using the Tersoff-Hamann approach with an s -wave tip (c),(d), a p -wave tip (e),(f), and an sp -wave mixed tip (g),(h). All images: $15\text{ \AA} \times 25\text{ \AA}$. Reprinted figure with permission from [Gross, L.; Moll, N.; Mohn, F.; Curioni, A.; Meyer, G.; Hanke, F.; Persson, M. *Phys. Rev. Lett.* **2011**, *107*, 086101.] Copyright 2011 by the American Physical Society.

1-3 Application of SPM to molecular device works

Although many researches have been devoted to the understanding of the electronic structure of a molecule, STM has also been applied to elucidate the single-molecule dynamics of molecular machines, such as azobenzene,¹⁸ diarylethene,^{19,20} quinone,²¹ rotaxane²² and so on.²³⁻²⁷ G. Rapenne, C. Joachim and S-W. Hla *et al.* designed an electrically-driven molecular rotor with four arms linked to a ferrocene group and succeeded in controlling the rotational motion by STM manipulation (Fig. 1-3).²⁸ When rotational motion is utilized as a wheel, continuous rotational motions allow a molecule to go and stop like a car on a surface (Fig. 1-4).²⁹ These outstanding researches are based on their accumulated works, which started from solution chemistry, to develop new systems of molecular machines.^{10,30-32} STM experiments prove their functionalities in the solid state, and moreover, at the single-molecule level.

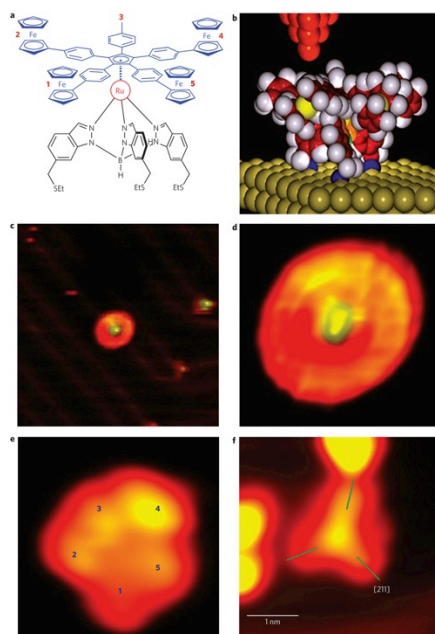


Fig. 1-2 STM images of the molecular machine comprising a five-arm rotor mounted on a molecular tripodal stator. Reprinted by permission from Macmillan Publishers Ltd: [Nature Nanotechnology] (Perera, U. G. E.; Ample, F.; Kersell, H.; Zhang, Y.; Vives, G.; Echeverria, J.; Grisolia, M.; Rapenne, G.; Joachim, C.; Hla, S.-W. *Nature Nanotech* **2013**, *8*, 46–51.), copyright 2013.

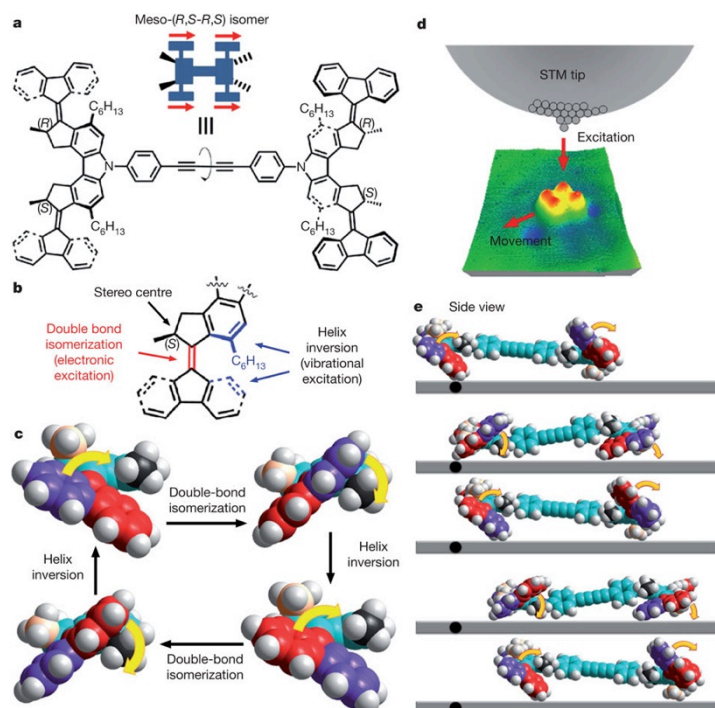


Fig. 1-3 The four-wheeled molecule. Reprinted by permission from Macmillan Publishers Ltd: [Nature] (Kudernac, T.; Ruangsupapichat, N.; Parschau, M.; Maciá, B.; Katsonis, N.; Harutyunyan, S. R.; Ernst, K.-H.; Feringa, B. L. *Nature* **2011**, *479*, 208–211.), copyright 2011.

1-4 Challenges for molecular device by SPM

Considering an ultimate goal of this research field as the application to molecular electronic devices, there are two issues to be addressed: slow scanning speed and operation at room temperature. The former has been discussed well until today and several methods were devised, making it possible to resolve ultrafast dynamics of molecules.³³⁻³⁹ The latter could be a problem because the tip position inevitably moves with respect to surface for thermal expansion of the components in STM machines. To bring molecular machine researches to more practical application, the molecule-based devices should be available at room temperature, as the conventional silicon-based devices actually are. Note that the high speed scanning may overcome this issue, room temperature observation, as well if resolution was high enough to visualize motion at low temperature. However, there is still concern for seeing small molecular motion.

1-5 Molecular motion in transition metal complexes

Controllable molecular motion plays a key role in biological systems such as myosin,⁴⁰⁻⁴² kinesin,^{43,44} dynein^{45,46} and ATP synthase.^{47,48} Since these biological molecular machines generate torque using chemical energy with high energy conversion efficiency, an artificial molecular machines that mimic their functions has attracted much attention. Feringa reported light-driven rotary motors based on *cis-trans* isomerization around a double bond.^{31,49} Stoddart,^{50,51} Kelly⁵² and other chemists also achieved significant milestones in this research field.^{2,53} Transition metal complexes are well studied as artificial molecular machines due to the unique redox activities and coordination geometries.⁵⁴⁻⁵⁷ Sauvage and co-workers synthesized the interlocked systems consisting of Cu complexes whose rings have two different coordination sites of bidentate and tridentate units. As the favored coordination number is different between Cu(I) and Cu(II) ions, the two units alternatively coordinates to the Cu center with the Cu(II/I) redox reaction (Fig. 1-4).⁵⁸⁻⁶⁰ Similar rotational motion was also achieved with a rotaxane containing Ru(II), which shows a structural rearrangement by light irradiation based on the formation of dissociative d-d*excited state.⁶¹

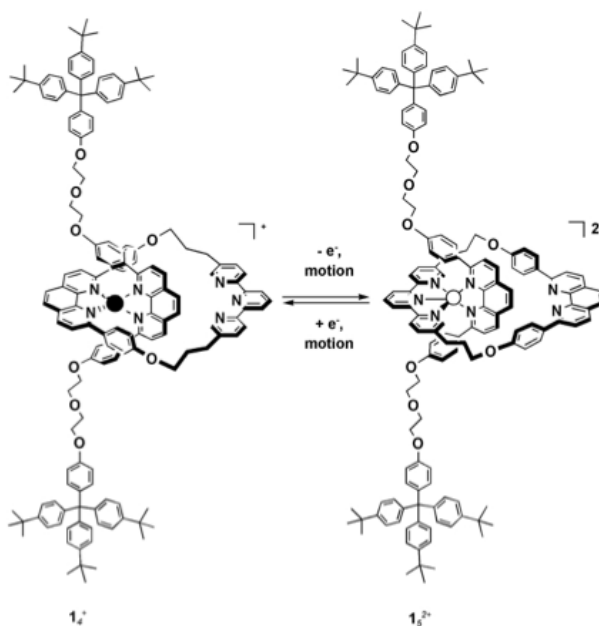


Fig. 1-4 A bistable molecular machine whose motion is controlled by the Cu(II/I) redox reaction. Reproduced from [Poleschak, I.; Kern, J.-M.; Sauvage, J.-P. A Copper-Complexed Rotaxane in Motion: Pirouetting of the Ring on the Millisecond Timescale. *Chem. Commun.* **2004**, 474–476.] with permission of The Royal Society of Chemistry.

1-6 Cu-pyrimidine system

A Cu(I) complex consisting of an asymmetrically substituted pyridylpyrimidine ligand takes two isomeric forms depending on the direction of the substitution as shown in Fig. 1-5.⁶²⁻⁷³ The two isomers are denoted by *i*- (inner) and *o*- (outer) isomer according to the position of the substitution on a pyrimidine ring. The rotational isomerization occurs fast in general, but the interconversion can be effectively slowed to enable its detection when the pyrimidine ring is confined in the space enclosed by two anthryl panels and a phenanthroline groups.^{74,75} The Cu complex favors a tetrahedral structure with 4-coordinated form in the Cu(I) state, on the other hand, it takes a square planar structure with 5- or 6-coordinated form in the Cu(II) state for Jahn-Teller effect.^{58,76,77} Consequently, the structural change of the Cu complex alters the Cu(II/I) redox potential. The oxidation potential of the *i*-isomer of a Cu complex with a methyl substitution, for example, is 0.17 V more positive than that of the *o*-isomer.^{19,20,62}

The rotation of this system can be driven by temperature⁶² and light,^{67,69} and furthermore, the motion can be detected as various kinds of outputs; for example, changes of rest potential,⁶² magnetic⁶³ and optical properties.⁶⁶

Note that it is the correlation between redox potential and structure that enables these functionalities within a simple and small molecular design.

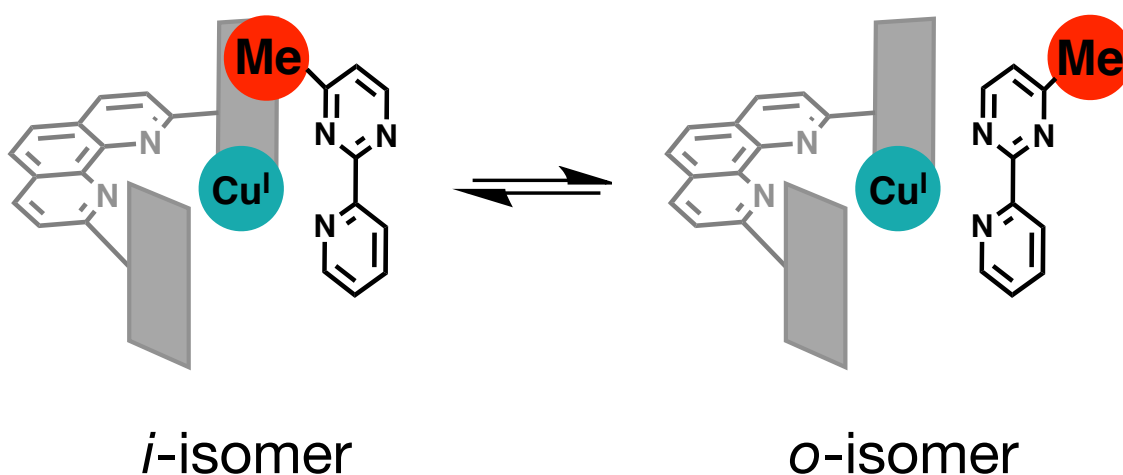


Fig. 1-5 Schematic of rotational equilibrium of a Cu-pyrimidine complex. The panels represent 9-anthryl groups.

1-7 Aim of this research

This research aims to develop the single-molecular system comprising the Cu-pyrimidine rotors. As described in the previous section, the rotational motion of this system affects the coordination environment around a Cu center. Hence, such small degree of motion can be detected by STM as the change of tunneling current, which is related to the electronic structure of a molecule.

The Cu-pyrimidine complexes were immobilized on the Au surface and its rotational behavior coupled with the Cu(II/I) redox reaction was investigated by cyclic voltammetry. It was first confirmed that the system certainly shows the rotational isomerization even on the Au surface, which is not a homogenous condition as in solution. An additional Cu complex tethered with a larger rotation unit was also prepared for comparison to determine if there is any specific effect of immobilization on the rotation dynamics. Their rotational behaviors were further discussed quantitatively based on the kinetic parameters obtained by the simulative analysis on the cyclic voltammograms.

Cyclic voltammetry revealed that this system works on Au surfaces and the rotation rate decreased compared with that in solution. These features strongly indicate the applicability of STM measurements. If the rotational motion can be visualized as the conductivity changes, the correlation between a molecular motion and electronic structure would be the promising approach to allow the small molecular machines to be accessible by STM.

The bistable Cu-pyrimidine systems were successfully functionalized on surface. The bipyrimidine ligand was employed to achieve a tristable system. The two rotational steps of the two rotors would result in the formation of three discrete isomers, if the two steps were not equivalent. The difference of two rotational behaviors was studied by ^1H NMR and cyclic voltammetry.

1-8 References

- (1) Aviram, A.; Ratner, M. A. *Chemical Physics Letters* **1974**, *29*, 277–283.
- (2) Balzani, V.; Credi, A.; Venturi, M. *Molecular Devices and Machines*; John Wiley & Sons, 2008.
- (3) Roldan, D.; Kaliginedi, V.; Cobo, S.; Kolivoska, V.; Bucher, C.; Hong, W.; Royal, G.; Wandlowski, T. *J. Am. Chem. Soc* **2013**, *135*, 5974–5977.
- (4) Namiki, K.; Sakamoto, A.; Murata, M.; Kume, S.; Nishihara, H. *Chemical Communications* **2007**, 4650.
- (5) Akutagawa, T.; Koshinaka, H.; Sato, D.; Takeda, S.; Noro, S.-I.; Takahashi, H.; Kumai, R.; Tokura, Y.; Nakamura, T. *Nat Mater* **2009**, *8*, 342–347.
- (6) Morimoto, M.; Miyasaka, H.; Yamashita, M.; Irie, M. *J. Am. Chem. Soc* **2009**, *131*, 9823–9835.
- (7) Liu, Z. *Science* **2003**, *302*, 1543–1545.
- (8) Lahann, J. *Science* **2003**, *299*, 371–374.
- (9) Green, J. E.; Choi, J. W.; Boukai, A.; Bunimovich, Y.; Johnston-Halperin, E.; DeLonno, E.; Luo, Y.; Sheriff, B. A.; Xu, K.; Shin, Y. S.; Tseng, H.-R.; Stoddart, J. F.; Heath, J. R. *Nature* **2007**, *445*, 414–417.
- (10) Fletcher, S. P.; Dumur, F.; Pollard, M. M.; Feringa, B. L. *Science* **2005**, *310*, 80–82.
- (11) Ito, H.; Saito, T.; Oshima, N.; Kitamura, N.; Ishizaka, S.; Hinatsu, Y.; Wakeshima, M.; Kato, M.; Tsuge, K.; Sawamura, M. *J. Am. Chem. Soc* **2008**, *130*, 10044–10045.
- (12) Zhang, G.; Lu, J.; Sabat, M.; Fraser, C. L. *J. Am. Chem. Soc* **2010**, *132*, 2160–2162.
- (13) Ulman, A. *Chem. Rev.* **1996**, *96*, 1533–1554.
- (14) Binnig, G.; Rohrer, H.; Gerber, C.; Weibel, E. *Phys. Rev. Lett.* **1983**, *50*, 120–123.
- (15) Schmaus, S.; Bagrets, A.; Nahas, Y.; Yamada, T. K.; Bork, A.; Bowen, M.; Beaurepaire, E.; Evers, F.; Wulfhekel, W. *Nature Nanotech* **2011**, *6*, 185–189.
- (16) Park, J.; Pasupathy, A. N.; Goldsmith, J. I.; Chang, C.; Yaish, Y.; Petta, J. R.; Rinkoski, M.; Sethna, J. P.; Abruña, H. D.; McEuen, P. L.; Ralph, D. C. *Nature* **2002**, *417*, 722–725.
- (17) Guédon, C. M.; Valkenier, H.; Markussen, T.; Thygesen, K. S.; Hummelen, J. C.; van der Molen, S. J. *Nature Nanotech* **2012**, *7*, 305–309.
- (18) Pathem, B. K.; Zheng, Y. B.; Payton, J. L.; Song, T.-B.; Yu, B.-C.; Tour, J. M.; Yang, Y.; Jensen, L.; Weiss, P. S. *J. Phys. Chem. Lett.* **2012**, *3*, 2388–2394.
- (19) Snegir, S. V.; Marchenko, A. A.; Yu, P.; Maurel, F.; Kapitanchuk, O. L.; Mazerat, S.; Lepeltier, M.; Léaustic, A.; Lacaze, E. *J. Phys. Chem. Lett.* **2011**, *2*, 2433–2436.

- (20) Arramel; Pijper, T. C.; Kudernac, T.; Katsonis, N.; van der Maas, M.; Feringa, B. L.; van Wees, B. J. *Nanoscale* **2013**.
- (21) Tsoi, S.; Griva, I.; Trammell, S. A.; Blum, A. S.; Schnur, J. M.; Lebedev, N. *ACS Nano* **2008**, *2*, 1289–1295.
- (22) Ye, T.; Kumar, A. S.; Saha, S.; Takami, T.; Huang, T. J.; Stoddart, J. F.; Weiss, P. S. *ACS Nano* **2010**, *4*, 3697–3701.
- (23) Pathem, B. K.; Zheng, Y. B.; Morton, S.; Petersen, M. Å.; Zhao, Y.; Chung, C.-H.; Yang, Y.; Jensen, L.; Nielsen, M. B.; Weiss, P. S. *Nano Lett.* **2013**, *13*, 337–343.
- (24) Pan, S.; Fu, Q.; Huang, T.; Zhao, A.; Wang, B.; Luo, Y.; Yang, J.; Hou, J. *Proc. Natl. Acad. Sci. U.S.A.* **2009**, *106*, 15259–15263.
- (25) Walch, H.; Leoni, T.; Guillermet, O.; Langlais, V.; Scheuermann, A.; Bonvoisin, J.; Gauthier, S. *Phys. Rev. B* **2012**, *86*, 075423.
- (26) Kühne, D.; Klappenberger, F.; Krenner, W.; Klyatskaya, S.; Ruben, M.; Barth, J. V. *Proc. Natl. Acad. Sci. U.S.A.* **2010**, *107*, 21332–21336.
- (27) Zhong, D.; Wedeking, K.; Chi, L.; Erker, G.; Fuchs, H. *Nano Lett.* **2009**, *9*, 4387–4391.
- (28) Perera, U. G. E.; Ample, F.; Kersell, H.; Zhang, Y.; Vives, G.; Echeverria, J.; Grisolia, M.; Rapenne, G.; Joachim, C.; Hla, S.-W. *Nature Nanotech* **2013**, *8*, 46–51.
- (29) Kudernac, T.; Ruangsupapichat, N.; Parschau, M.; Maciá, B.; Katsonis, N.; Harutyunyan, S. R.; Ernst, K.-H.; Feringa, B. L. *Nature* **2011**, *479*, 208–211.
- (30) Browne, W. R.; Feringa, B. L. *Nature Nanotech* **2006**, *1*, 25–35.
- (31) Koumura, N.; Zijlstra, R. W.; van Delden, R. A.; Harada, N.; Feringa, B. L. *Nature* **1999**, *401*, 152–155.
- (32) Vives, G.; Carella, A.; Launay, J.-P.; Rapenne, G. *Coordination Chemistry Reviews* **2008**, *252*, 1451–1459.
- (33) Yoshida, S.; Aizawa, Y.; Wang, Z.-H.; Oshima, R.; Mera, Y.; Matsuyama, E.; Oigawa, H.; Takeuchi, O.; Shigekawa, H. *Nature Nanotech* **2014**, *9*, 588–593.
- (34) Loth, S.; Etzkorn, M.; Lutz, C. P.; Eigler, D. M.; Heinrich, A. J. *Science* **2010**, *329*, 1628–1630.
- (35) Teufel, J. D.; Donner, T.; Castellanos-Beltran, M. A.; Harlow, J. W.; Lehnert, K. W. *Nature Nanotech* **2009**, *4*, 820–823.
- (36) Kemiktarak, U.; Ndukum, T.; Schwab, K. C.; Ekinci, K. L. *Nature* **2007**, *450*, 85–88.
- (37) Besenbacher, F.; Lægsgaard, E.; Stensgaard, I. *Materials Today* **2005**, *8*, 26–30.
- (38) Mamin, H. J.; Birk, H.; Wimmer, P.; Rugar, D. *J. Appl. Phys.* **1994**, *75*, 161.

- (39) Nunes, G.; Freeman, M. R. *Science* **1993**, *262*, 1029–1032.
- (40) Sweeney, H. L.; Houdusse, A. *Curr. Opin. Cell Biol.* **2007**, *19*, 57–66.
- (41) Ménétrey, J.; Bahloul, A.; Wells, A. L.; Yengo, C. M.; Morris, C. A.; Sweeney, H. L.; Houdusse, A. *Nature* **2005**, *435*, 779–785.
- (42) Sweeney, H. L.; Wells, A. L.; Lin, A. W.; Chen, L.-Q.; Safer, D.; Cain, S. M.; Hasson, T.; Carragher, B. O.; Milligan, R. A. *Nature* **1999**, *401*, 505–508.
- (43) Vale, R. D.; Reese, T. S.; Sheetz, M. P. *Cell* **1985**, *42*, 39–50.
- (44) Nogales, E.; Whittaker, M.; Milligan, R. A.; Downing, K. H. *Cell* **1999**, *96*, 79–88.
- (45) Kon, T.; Oyama, T.; Shimo-Kon, R.; Imamula, K.; Shima, T.; Sutoh, K.; Kurisu, G. *Nature* **2012**, *484*, 345–350.
- (46) Roberts, A. J.; Kon, T.; Knight, P. J.; Sutoh, K.; Burgess, S. A. *Nature Reviews Molecular Cell Biology* **2013**, *14*, 713–726.
- (47) Junge, W.; Sielaff, H.; Engelbrecht, S. *Nature* **2009**, *459*, 364–370.
- (48) Noji, H.; Yasuda, R.; Yoshida, M.; Kinosita, K. *Nature* **1997**, *386*, 299–302.
- (49) van Delden, R. A.; Wiel, ter, M. K. J.; Pollard, M. M.; Vicario, J.; Koumura, N.; Feringa, B. L. *Nature* **2005**, *437*, 1337–1340.
- (50) Collier, C. P.; Mattersteig, G.; Wong, E. W.; Luo, Y.; Beverly, K.; Sampaio, J.; Raymo, F. M.; Stoddart, J. F.; Heath, J. R. *Science* **2000**, *289*, 1172–1175.
- (51) Collier, C.; Wong, E.; Belohradsky, M.; Raymo, F.; Stoddart, J.; Kuekes, P.; Williams, R.; Heath, J. *Science* **1999**, *285*, 391–394.
- (52) Kelly, T. R.; De Silva, H.; Silva, R. A. *Nature* **1999**, *401*, 150–152.
- (53) Balzani, V.; Credi, A.; Venturi, M. *Chemphyschem* **2008**, *9*, 202–220.
- (54) Muraoka, T.; Kinbara, K.; Aida, T. *Nature* **2006**, *440*, 512–515.
- (55) Kinbara, K.; Aida, T. *Chem. Rev.* **2005**, *105*, 1377–1400.
- (56) Hiraoka, S.; Shiro, M.; Shionoya, M. *J. Am. Chem. Soc.* **2004**, *126*, 1214–1218.
- (57) Hiraoka, S.; Harano, K.; Tanaka, T.; Shiro, M.; Shionoya, M. *Angew. Chem. Int. Ed. Engl.* **2003**, *42*, 5182–5185.
- (58) Poleschak, I.; Kern, J.-M.; Sauvage, J.-P. *Chem. Commun. (Camb.)* **2004**, 474–476.
- (59) Armaroli, N.; Balzani, V.; Collin, J.-P.; Gaviña, P.; Sauvage, J.-P.; Ventura, B. *J. Am. Chem. Soc.* **1999**, *121*, 4397–4408.
- (60) Joosten, A.; Trolez, Y.; Collin, J.-P.; Heitz, V.; Sauvage, J.-P. *J. Am. Chem. Soc.* **2012**, *134*, 1802–1809.
- (61) Mobian, P.; Kern, J.-M.; Sauvage, J.-P. *Angew. Chem.* **2004**, *116*, 2446–2449.

- (62) Nomoto, K.; Kume, S.; Nishihara, H. *J. Am. Chem. Soc.* **2009**, *131*, 3830–3831.
- (63) Kume, S.; Nomoto, K.; Kusamoto, T.; Nishihara, H. *J. Am. Chem. Soc.* **2009**, *131*, 14198–14199.
- (64) Kume, S.; Nishihara, H. *Dalton Trans.* **2011**, *40*, 2299–2305.
- (65) Kume, S.; Nishihara, H. *Chemical Communications* **2011**, *47*, 415–417.
- (66) Nishikawa, M.; Nomoto, K.; Kume, S.; Inoue, K.; Sakai, M.; Fujii, M.; Nishihara, H. *J. Am. Chem. Soc.* **2010**, *132*, 9579–9581.
- (67) Nishikawa, M.; Nomoto, K.; Kume, S.; Nishihara, H. *J. Am. Chem. Soc.* **2012**, *134*, 10543–10553.
- (68) Nishikawa, M.; Nomoto, K.; Kume, S.; Nishihara, H. *Inorg. Chem.* **2013**, *52*, 369–380.
- (69) Nishikawa, M.; Takara, Y.; Hattori, Y.; Nomoto, K.; Kusamoto, T.; Kume, S.; Nishihara, H. *Inorg. Chem.* **2013**, *52*, 8962–8970.
- (70) Nishikawa, M.; Kume, S.; Nishihara, H. *Phys. Chem. Chem. Phys.* **2013**.
- (71) Hattori, Y.; Nishikawa, M.; Kusamoto, T.; Kume, S.; Nishihara, H. *Inorg. Chem.* **2014**, *53*, 2831–2840.
- (72) Hattori, Y.; Nishikawa, M.; Kusamoto, T.; Kume, S.; Nishihara, H. *Chem. Lett.* **2014**, *43*, 1037–1039.
- (73) Takara, Y.; Kusamoto, T.; Masui, T.; Nishikawa, M.; Kume, S.; Nishihara, H. *Chemical Communications* **2015**, *51*, 2896–2898.
- (74) Schmittel, M.; Michel, C.; Liu, S.-X.; Schildbach, D.; Fenske, D. *European Journal of Inorganic Chemistry* **2001**, *2001*, 1155–1166.
- (75) Schmittel, M.; Lüning, U.; Meder, M.; Ganz, A.; Michel, C.; Herderich, M. *Heterocyclic Communications* **1997**, *3*, 493–498.
- (76) Rorabacher, D. B. *Chem. Rev.* **2004**, *104*, 651–698.
- (77) Ruthkosky, M.; Kelly, C. A.; Castellano, F. N.; Meyer, G. J. *Coordination Chemistry Reviews* **1998**, *171*, 309–322.

Chapter 2

Electrochemical Analysis of Cu-pyrimidine Complexes Immobilized on Au Surface

2-1 Introduction

This chapter describes the rotational behavior of Cu-pyrimidine complexes on the Au surface. Since the Cu-pyrimidine system was first formulated, the studies had been focused on a solution state, and hence the application to the solid state is of significance not only to STM observation of individual molecules, but also to bringing its functionality close to practical molecular machines working under normal environmental conditions.

The questions to be clarified in this chapter are the following fundamental points; i) can this system work in a heterogeneous system? ii) can the rotation be detected by the gold electrode through the redox of Cu(II/I)? and iii) does any characteristic effect exist on dynamics by immobilization?

This chapter consists of the preparation, characterization and electrochemical analysis of two kinds of Cu-pyrimidine complexes immobilized on the Au surface. Cyclic voltammetry revealed that the rotation takes place on the Au surface. The differences of the rotational behaviors on surface and in solution are discussed quantitatively based on thermodynamic and kinetic parameters obtained by simulative analysis.

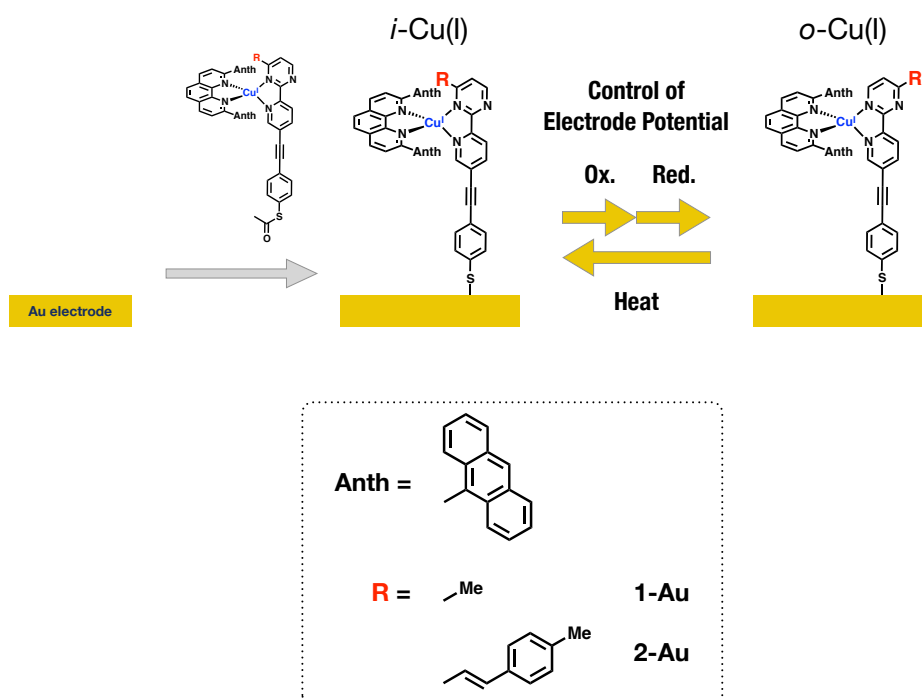


Fig. 2-1 Schematic of the immobilized ring rotation system.

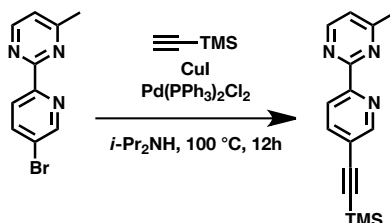
2-2 Experimental

2-2-1 Materials

Tetra-*n*-butylammonium hexafluoro phosphate (purchased from Tokyo Chemical Industry) was recrystallized from HPLC-grade ethanol and dried under vacuum for 24 h. 2,9-Bis(9-anthracenyl)-1,10-phenanthroline (L_{Anth2}),¹ 2-(5-bromopyridyl)-4-methylpyrimidine,² *S*-acetyl-4-iodothiophenol³ and 5-bromo-6'-methyl-2,2'-bipyridine⁴ were prepared according to literature methods. CH_2Cl_2 and THF were purified by Glass Contour Solvent Purification system (Nikko Hansen & Co., Ltd.). Other chemicals were used as purchased.

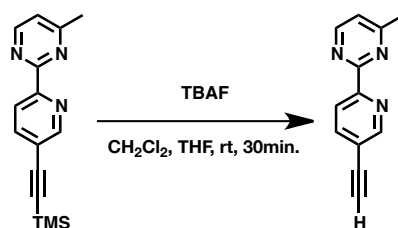
2-2-2 Synthesis

4-Methyl-2-(5-((trimethylsilyl)ethynyl)pyridin-2-yl)pyrimidine (5)



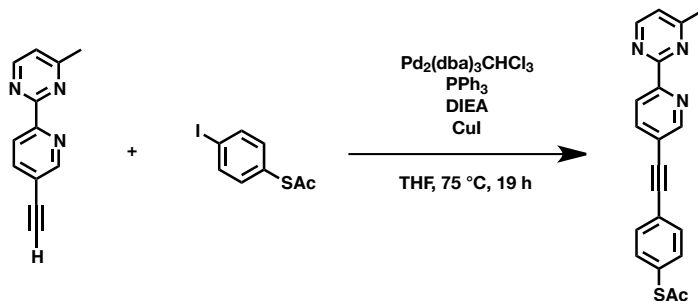
Under a nitrogen atmosphere, 2-(5-bromopyridyl)-4-methylpyrimidine (1.30 g, 5.19 mmol), copper(I) iodide (148 mg, 0.777 mmol) and $Pd(PPh_3)_2Cl_2$ (364 mg, 0.519 mmol) were added to *i*-Pr₂NH (50 mL). Trimethylsilylacetylene (1.21 mL, 8.69 mmol) was added and the solution was stirred for 12 h at 90°C. The resulted black solution was filtered and washed with dichloromethane. The filtrate was evaporated and the crude product was purified with alumina column chromatography eluted with ethyl acetate/hexane (1:5v/v) to give a white powder of **5**. Yield: 1.09 g (79 %). ¹H NMR (500 MHz, CDCl₃) δ 8.88 (d, *J* = 2.1 Hz, 1H, py), 8.75 (d, *J* = 5.0 Hz, 1H, pm), 8.48 (d, *J* = 8.2 Hz, 1H, py), 7.90 (dd, *J* = 8.2, 2.1 Hz, 1H, py), 7.17 (d, *J* = 5.0 Hz, 1H, pm), 2.66 (s, 3H, pm-Me), 0.28 (s, 9H, Si-Me).

2-(5-Ethynylpyridin-2-yl)-4-methylpyrimidine (6)



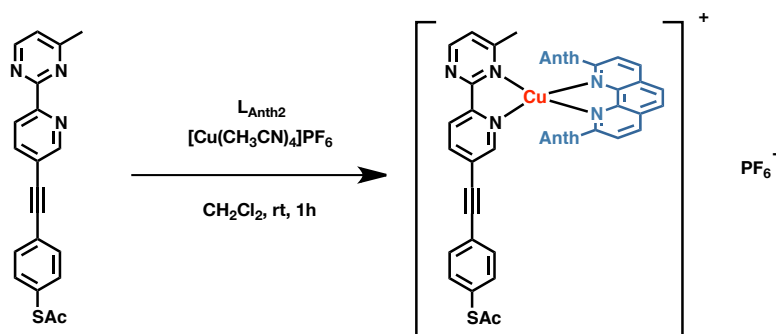
5 (1.09 g, 4.06 mmol) and tetra-*n*-butylammonium fluoride (4.1 ml, 1M in THF) were stirred in CH₂Cl₂ for 30 min at room temperature. The solution was filtered, and the filtrate was evaporated. The crude product was purified with alumina column chromatography eluted with CH₂Cl₂. Yield: 0.759 g (96 %). ¹H NMR (500 MHz, CDCl₃) δ 8.92 (d, *J* = 2.1 Hz, 1H, py), 8.75 (d, *J* = 5.0 Hz, 1H, pm), 8.50 (d, *J* = 8.2 Hz, 1H, py), 7.93 (dd, *J* = 8.2, 2.1 Hz, 1H, py), 7.19 (d, *J* = 5.0 Hz, 1H, pm), 3.33 (s, 1H, ethynyl), 2.66 (s, 3H, pm-Me).

S-acetyl-4-(6-(4-methylpyrimidin-2-yl)pyridin-3-yl)ethynylthiophenol (pmpySAc) (7)



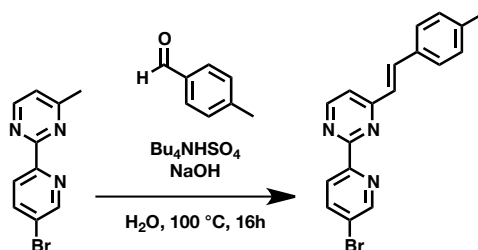
Under a nitrogen atmosphere, *S*-acetyl-4-iodothiophenol (510 mg, 1.83 mmol), tris(dibenzylideneacetone)dipalladium (41 mg, 0.45 mmol), triphenylphosphine (101 mg, 0.39 mmol), copper(I) iodide (34 mg, 0.179 mmol) were added to THF (20 ml). *i*-Pr₂NEt (2.7 ml, 16 mmol) and **6** (361 mg, 1.85 mmol) were added and the reaction mixture was stirred for 19 h at 60°C. The solution was filtered, and the filtrate was evaporated. The residue was purified with silica column chromatography eluted with ethyl acetate to give a yellow-white solid. Yield: 91.7 mg (14 %). ¹H NMR (500 MHz, CDCl₃) δ 8.97 (d, *J* = 2.1 Hz, 1H, py), 8.77 (d, *J* = 5.0 Hz, 1H, pm), 8.55 (d, *J* = 8.2 Hz, 1H, py), 7.98 (dd, *J* = 8.2, 2.1 Hz, 1H, py), 7.61 (d, *J* = 8.4 Hz, 2H, ph), 7.44 (d, *J* = 8.4 Hz, 2H, ph), 7.20 (d, *J* = 5.0 Hz, 1H, pm), 2.68 (s, 3H, pm-Me), 2.45 (s, 3H, CO-Me). ESI-TOF-MS *m/z* 346.09 (calcd. for [M+H⁺], 346.10).

[Cu(pmpySAc)(L_{Anth2})]PF₆ (**1**·PF₆)



Under a nitrogen atmosphere, 2,9-bis(9-anthracenyl)-1,10-phenanthroline (L_{Anth2}, 31 mg, 58 μ mol) and [Cu(CH₃CN)₄]PF₆ (22 mg, 58 μ mol) were stirred for 30 min in dichloromethane. To the resulted orange clear solution, pmpySAc (20 mg, 58 μ mol) was added and the solution immediately changed to deep red. After filtration, diethyl ether was added to the filtrate to precipitate **1**·PF₆ as a deep red solid. Yield: 46 mg (73 %). ¹H NMR (500 MHz, (CD₃)₂CO) δ 9.25 (d, J = 8.2 Hz, py), 9.22 (d, J = 8.2 Hz, pm), 8.64 (s, py), 8.63 (s, py), 8.45 (d, J = 8.2 Hz, ph), 8.43 (d, J = 8.2 Hz, ph), 8.26 (d, J = 5.0 Hz, pm), 8.04 (s, *i*-Anth), 8.03 (s, *o*-Anth), 7.75-7.73 (m), 7.72-7.68 (m), 7.66 (d, J = 1.9 Hz, py), 7.65-7.61 (m), 7.57 (m), 7.41 (m), 7.34-7.29 (m), 7.23-7.18(m), 7.17-7.12 (m), 6.63 (d, J = 4.9 Hz, pm), 6.43 (d, J = 5.4 Hz, pm), 2.48 (m, CO-*i,o*-Me), 2.38 (s, pm-*o*-Me), 1.61 (s, pm-*i*-Me). ESI-TOF-MS m/z 940.2142 (calcd. for [M-PF₆]⁺, 940.2171).

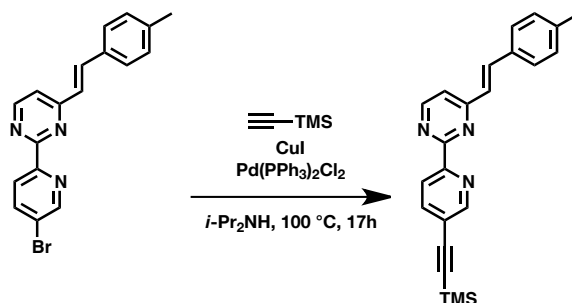
(*E*)-2-(5-bromopyridin-2-yl)-4-(4-methylstyryl)pyrimidine (**8**)



A mixture of 2-(5-bromopyridin-2-yl)-4-methylpyrimidine (750 mg, 3.00 mmol) and *p*-tolualdehyde (3.05 ml, 25.9 mmol) in an aqueous solution of sodium hydroxide (1M, 3.3 ml) and tetrabutylammonium hydrogen sulfate (24 mg, 0.30 mmol) was refluxed for 16 h. After cooling the resulted mixture was extracted with CH₂Cl₂ and purified with alumina column chromatography eluted with CH₂Cl₂/hexane (1:1v/v) to give a yellow-white solid. Yield: 544 mg (51 %). ¹H NMR (500 MHz, CDCl₃) δ 8.90 (d, J =

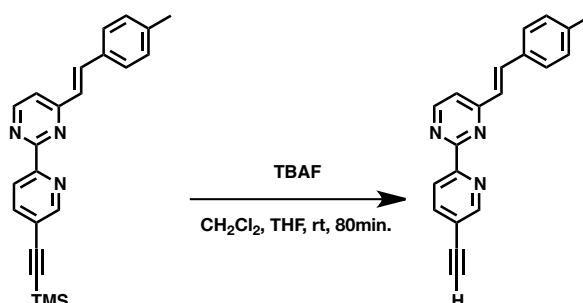
2.4 Hz, 1H, py), 8.84 (d, $J = 5.2$ Hz, 1H, pm), 8.52 (d, $J = 8.5$ Hz, 1H, py), 8.03 (dd, $J = 8.5$, 2.4 Hz, 1H, py), 7.93 (d, $J = 16$ Hz, 1H, vinylene), 7.55 (d, $J = 8.1$ Hz, 2H, tol), 7.36 (d, $J = 5.2$ Hz, 1H, pm), 7.24 (d, $J = 8.0$ Hz, 2H, tol), 7.17 (d, $J = 16$ Hz, 1H, vi), 2.40 (s, 3H, tol-Me).

(E)-4-(4-methylstyryl)-2-(5-((trimethylsilyl)ethynyl)pyridin-2-yl)pyrimidine (9)



Under a nitrogen atmosphere, **7** (487 mg, 1.38 mmol), copper(I) iodide (39.7 mg, 0.208 mmol) and Pd(PPh₃)₂Cl₂ (93.6 mg, 0.133 mmol) were added to *i*-Pr₂NH (24 mL). To the solution, trimethylsilylacetylene (0.325 mL, 2.34 mmol) was added and stirred for 17 h at 100°C. The resulted black solution was filtered and washed with CH₂Cl₂. The filtrate was evaporated and the crude product was purified with alumina column chromatography eluted with ethyl acetate/hexane (1:1v/v) to give a yellow-white powder of **9**. Yield: 247 mg (48 %). ¹H NMR (500 MHz, CDCl₃) δ 8.90 (d, $J = 2.0$ Hz, 1H, py), 8.85 (d, $J = 5.2$ Hz, 1H, pm), 8.57 (d, $J = 8.2$ Hz, 1H, py), 7.95-7.92 (m, 2H, py, vi), 7.55 (d, $J = 8.1$ Hz, 2H, tol), 7.34 (d, $J = 5.2$ Hz, 1H, pm), 7.24 (d, $J = 8.0$ Hz, 2H, tol), 7.18 (d, $J = 16$ Hz, 1H, vi), 2.40 (s, 3H, tol-Me), 0.30 (s, 9H, Si-Me).

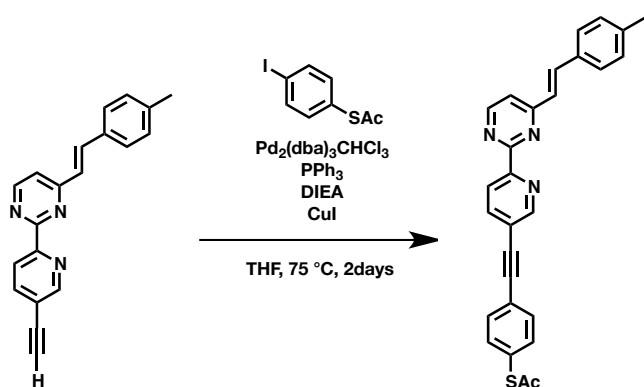
(E)-2-(5-ethynylpyridin-2-yl)-4-(4-methylstyryl)pyrimidine (10)



9 (247 mg, 0.668 mmol) and tetra-*n*-butylammonium fluoride (1.45 ml, 1M in THF) were stirred in CH₂Cl₂ for 80 min at room temperature. The solution was filtered, and the filtrate was evaporated. The crude product of **10** was purified with alumina column

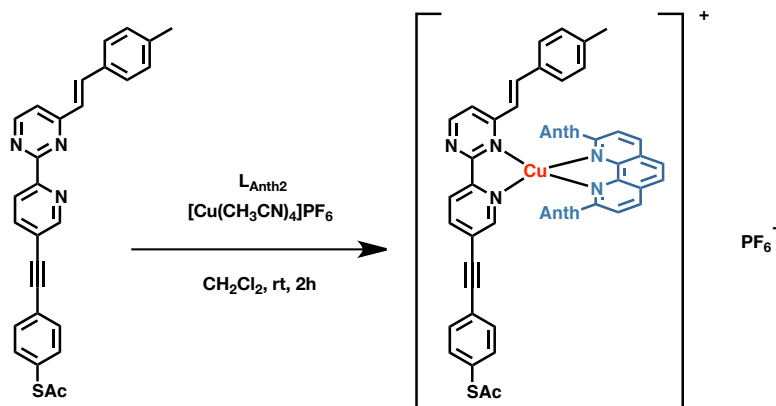
chromatography eluted with CH₂Cl₂. Yield: 197 mg (99 %). ¹H NMR (500 MHz, CDCl₃) δ 8.95 (d, *J* = 2.0 Hz, 1H, py), 8.86 (d, *J* = 5.2 Hz, 1H, pm), 8.60 (d, *J* = 8.2 Hz, 1H, py), 7.97 (dd, *J* = 8.2, 2.1 Hz, 1H, py), 7.94 (d, *J* = 16 Hz, 1H, vi), 7.55 (d, *J* = 8.1 Hz, 2H, tol), 7.35 (d, *J* = 5.2 Hz, 1H, pm), 7.24 (d, *J* = 8.0 Hz, 2H, tol), 7.18 (d, *J* = 16 Hz, 1H, vi), 3.35 (s, 1 H, ethynyl), 2.40 (s, 3H, tol-Me).

(*E*)-*S*-(4-(((6-(4-(4-methylstyryl)pyrimidin-2-yl)pyridin-3-yl)ethynyl)phenyl)ethanethioate (TolpmpySAc) (11)



Under a nitrogen atmosphere, *S*-acetyl-4-iodothiophenol (93.0 mg, 0.334 mmol), tris(dibenzylideneacetone)dipalladium (9.6 mg, 0.017 mmol), triphenylphosphine (18 mg, 0.069 mmol), copper(I) iodide (3.7 mg, 0.019 mmol) were added to THF (8.0 ml). *i*-Pr₂NEt (0.53 ml, 3.0 mmol) and **10** (100 mg, 0.336 mmol) were added and the reaction mixture was stirred for 40 h at 60°C. The solution was filtered, and the solvent was evaporated. A yellow-white solid of **11** was given by purification with silica column chromatography eluted with CH₂Cl₂ followed by recrystallization (CH₂Cl₂/hexane). Yield: 37.5 mg (25 %). ¹H NMR (500 MHz, CDCl₃) δ 8.99 (d, *J* = 2.0 Hz, 1H, py), 8.87 (d, *J* = 5.1 Hz, 1H, pm), 8.63 (d, *J* = 8.2 Hz, 1H, py), 8.01 (dd, *J* = 8.2, 2.1 Hz, 1H, py), 7.95 (d, *J* = 16 Hz, 1H, vi), 7.62 (d, *J* = 8.1 Hz, 2H, ph), 7.56 (d, *J* = 8.0 Hz, 2H, tol), 7.45 (d, *J* = 8.1 Hz, 2H, ph), 7.36 (d, *J* = 5.2 Hz, 1H, pm), 7.24 (d, *J* = 8.0 Hz, 2H, tol), 7.19 (d, *J* = 16 Hz, 1H, vi), 2.46 (s, 1 H, CO-Me), 2.40 (s, 3H, tol-Me).

[Cu(TolpmpySAC)(L_{Anth2})]PF₆ (2·PF₆)



Under a nitrogen atmosphere, 2,9-bis(9-anthracenyl)-1,10-phenanthroline²⁵ (L_{Anth2}, 29 mg, 54 μmol) and [Cu(CH₃CN)₄]PF₆ (20 mg, 54 μmol) were stirred for 30 min in dichloromethane. To the resulted orange clear solution, tolmpySAC (24 mg, 54 μmol) was added and the solution immediately changed to deep red. After filtration, diethyl ether was added to the filtrate to precipitate **2**·PF₆ as a deep red solid. Yield: 40.3 mg (61 %). ¹H NMR (500 MHz, (CD₃)₂CO) δ 9.29 (d, *J* = 8.2 Hz, phen), 9.23 (d, *J* = 8.1 Hz, phen), 8.77 (s, phen), 8.63 (s, phen), 8.45 (m, phen), 8.29 (d, *J* = 5.2 Hz, pm), 8.04 (s, *i*-Anth), 8.02 (s, *o*-Anth), 7.97 (d, *J* = 16 Hz, vi), 7.82 (d, *J* = 8.2 Hz, *o*-py), 7.78-7.75 (m), 7.74-7.68 (m), 7.65-7.55 (m), 7.40-7.32 (m), 7.30-7.25 (m), 7.25-6.99 (m), 6.83-6.78(m), 6.60-6.56 (m), 6.13 (d, *J* = 17 Hz, vi), 2.49 (s, CO-*i*-Me), 2.48 (s, CO-*o*-Me), 2.43 (s, tol-*o*-Me), 2.33 (s, tol-*i*-Me). ESI-TOF-MS *m/z* 1042.2640 (calcd. for [M-PF₆]⁺, 1042.2639).

2-2-3 Experimental apparatus

X-ray Structural Analysis

A single crystal of $1 \cdot \text{PF}_6 \cdot \text{CH}_2\text{Cl}_2$ was obtained by diffusing hexane into a dichloromethane solution of $1 \cdot \text{PF}_6$. The diffraction data for $1 \cdot \text{PF}_6 \cdot \text{CH}_2\text{Cl}_2$ were collected at 113 K on a AFC10 diffractometer with a Rigaku Saturn CCD system equipped with a rotating-anode X-ray generator that emitted graphite-monochromated MoK_α radiation ($\lambda = 0.7107 \text{ \AA}$). Lorentz-polarization and numerical absorption corrections were performed with the program Crystal Clear 1.3.6. The structure was solved by the direct method using SIR 92 program⁵ and refined against F^2 using SHELXL-97.⁶ WinGX software was used to prepare the material for publication.⁷

Instrumentation

^1H NMR spectra were recorded with a Bruker DRX500 spectrometer. ESI-TOF mass spectra were recorded using a Micromass LCT spectrometer. MALDI-TOF mass spectra were recorded using a Shimadzu/KRATOS AXIMA-CFR spectrometer. X-ray photoelectron spectra were measured with PHI5000 VersaProbe (ULVAC-PHI). Monochromatic Al $\text{K}\alpha$ (20 kV, 100 W) was used as the X-ray source. Exit angle was set to 15° and 45° . All spectra were calibrated according to the peak for Au $4f_{7/2}$ at 83.8 eV. Cyclic voltammograms was recorded with ALS 750A electrochemical analyzers (BAS. Co., Ltd.). The working electrode was a 3 mm ϕ glassy carbon disc embedded in glass, a platinum wire served as the auxiliary electrode, and the reference electrode was an Ag^+/Ag electrode (a silver wire immersed in 0.1 M $^n\text{Bu}_4\text{NClO}_4/0.01 \text{ M AgClO}_4/\text{CH}_3\text{CN}$). The solutions were deoxygenated with pure argon before measurement. Cyclic voltammograms of $1 \cdot \text{PF}_6$ and $2 \cdot \text{PF}_6$ were simulated with the BASi Digisim 3.03a software, based on two independent double step electron transfer systems. Electrochemical measurements of **1-Au** and **2-Au** were carried out using a Au/mica (electrode area: 0.264 cm^2) working electrode covered by a metal complex film, a Pt wire counter electrode, and an Ag^+/Ag reference electrode in a standard one-compartment cell.

Preparation of SAMs

Au/mica substrates were annealed with a hydrogen flame just before use. This treatment gave a surface dominated by Au(111) plane. After immersing the substrates

into 0.1 mM dichloromethane solutions of complexes with given immersion times (15 min for **1-Au** and 30 min for **2-Au**), the substrates were taken from the solutions, rinsed with clean CH₂Cl₂, and dried with nitrogen flush.

2-3 Results and discussion

2-3-1 X-ray structural analysis

Single crystals of $\mathbf{1}\cdot\text{PF}_6$ were obtained by diffusing 1-hexane into the dichloromethane solution of $\mathbf{1}\cdot\text{PF}_6$. X-ray structural analysis reveals that crystalline $\mathbf{1}\cdot\text{PF}_6$ exists as the *i*-isomer without disorder (Fig. 2-2, Table 2-1). The pyridylpyrimidine ligand is bound by two anthryl moieties and show π - π interaction with one of the anthryl group with the distance of 3.5 nm. The features mentioned above are commonly observed in our previous Cu-pyridylpyrimidine complexes.^{8,9} The crystal contains one dichloromethane molecule used as solvent. The high stability of *i*-isomer is considered to be derived from the induction effect of a methyl group.^{8,10}

Dichloroethane was used instead of dichloromethane for the preparation of single crystals of $\mathbf{2}\cdot\text{PF}_6$ (Fig. 2-3, Table 2-1). It was turned out that $\mathbf{2}\cdot\text{PF}_6$ also exists as the *i*-isomer in spite of the bulky substitution, and thus the induction effect of the vinyl group, which is smaller than that of a methyl group due to the less extended sp^2 configuration, is still large enough to exceed the steric effect.

Table 2-1 Crystallographic data of **1·PF₆** and **2·PF₆**

	1·PF₆·CH₂Cl₂	2·PF₆
Empirical formula	C ₆₁ H ₄₁ Cl ₂ CuF ₆ N ₅ OPS	C ₆₈ H ₄₅ CuF ₆ N ₅ OPS
Formula weight	1171.46	1335.15
Crystal system	monoclinic	triclinic
<i>a</i> / Å	11.740(5)	11.467(5)
<i>b</i> / Å	36.652(5)	16.953(5)
<i>c</i> / Å	12.039(5)	19.335(5)
α / °	90	73.567(5)
β / °	94.294(5)	83.876(5)
γ / °	90	79.884(5)
<i>V</i> / Å ³	5165.77	3542.67
Space group	<i>P</i> 2 ₁ / <i>c</i>	<i>P</i> -1
<i>Z</i>	4	2
λ / Å	0.7107	0.7107
<i>T</i> / K	113	93
μ / mm ⁻¹	0.669	0.533
ρ_{calcd} / g cm ⁻³	1.506	1.253
<i>R</i> ₁ ^[a]	0.0563	0.1325
<i>wR</i> ₂ ^[b]	0.1534	0.3929
<i>GOF</i> ^[c]	1.065	0.932

[a] $R_1 = \Sigma||F_o| - |F_c|| / \Sigma|F_o|$ ($I > 2\sigma(I)$). [b] $wR_2 = [\Sigma(w(F_o^2 - F_c^2)^2) / \Sigma w(F_o^2)^2]^{1/2}$ ($I > 2\sigma(I)$). [c] $GOF = [\Sigma(w(F_o^2 - F_c^2)^2) / \Sigma(N^r - N^p)^2]$.

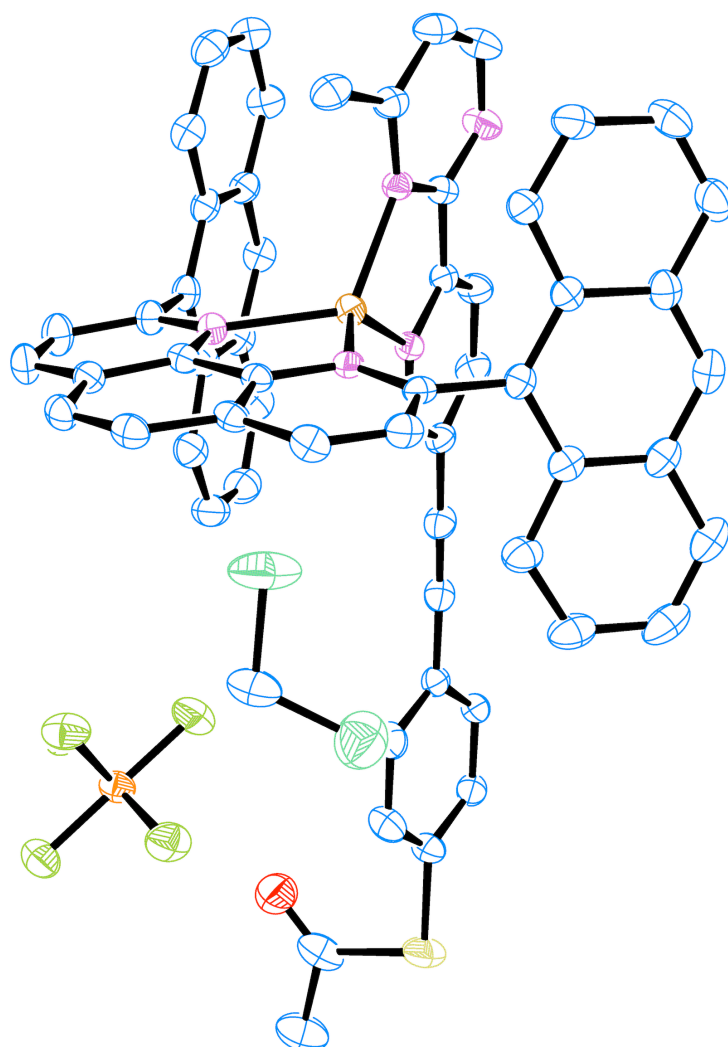


Fig. 2-2 ORTEP view of $1 \cdot \text{PF}_6 \cdot \text{CH}_2\text{Cl}_2$. The displacement ellipsoids are drawn at 50% probability level (blue, C; yellow, S; light orange, Cu; pink, N; green, Cl; yellow green, F; orange, P; H atoms are omitted for clarity).

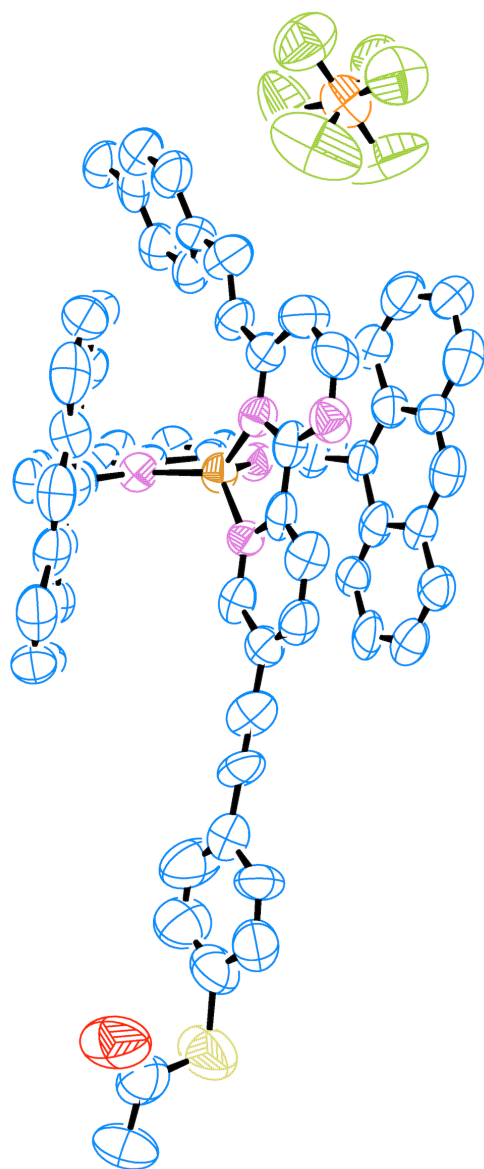


Fig. 2-3 ORTEP view of $2 \cdot \text{PF}_6$. The displacement ellipsoids are drawn at 50% probability level (blue, C; yellow, S; light orange, Cu; pink, N; yellow green, F; orange, P; H atoms are omitted for clarity).

2-3-2 $^1\text{H-NMR}$ measurements in solution state

$^1\text{H-NMR}$ spectra of $\mathbf{1}\cdot\text{PF}_6$ taken at room temperature in acetone- d_6 are shown in Fig. 2-4. The spectra showed two signals around 6.5 ppm that were assigned to the protons at 5-positions of pyrimidine rings of two isomers, considering the shielding effect of the Cu(I) center.⁸ A molar ratio of two isomers in the equilibrium state estimated from the ratio of integrated values was $o : i = 4 : 6$.

The ratio of two isomers calculated from $^1\text{H-NMR}$ spectra of $\mathbf{2}\cdot\text{PF}_6$, $o : i = 5 : 5$, indicated that the *i*-isomer became thermodynamically unstable, due to the larger steric effect of the bulky rotor, as we previously reported.¹¹

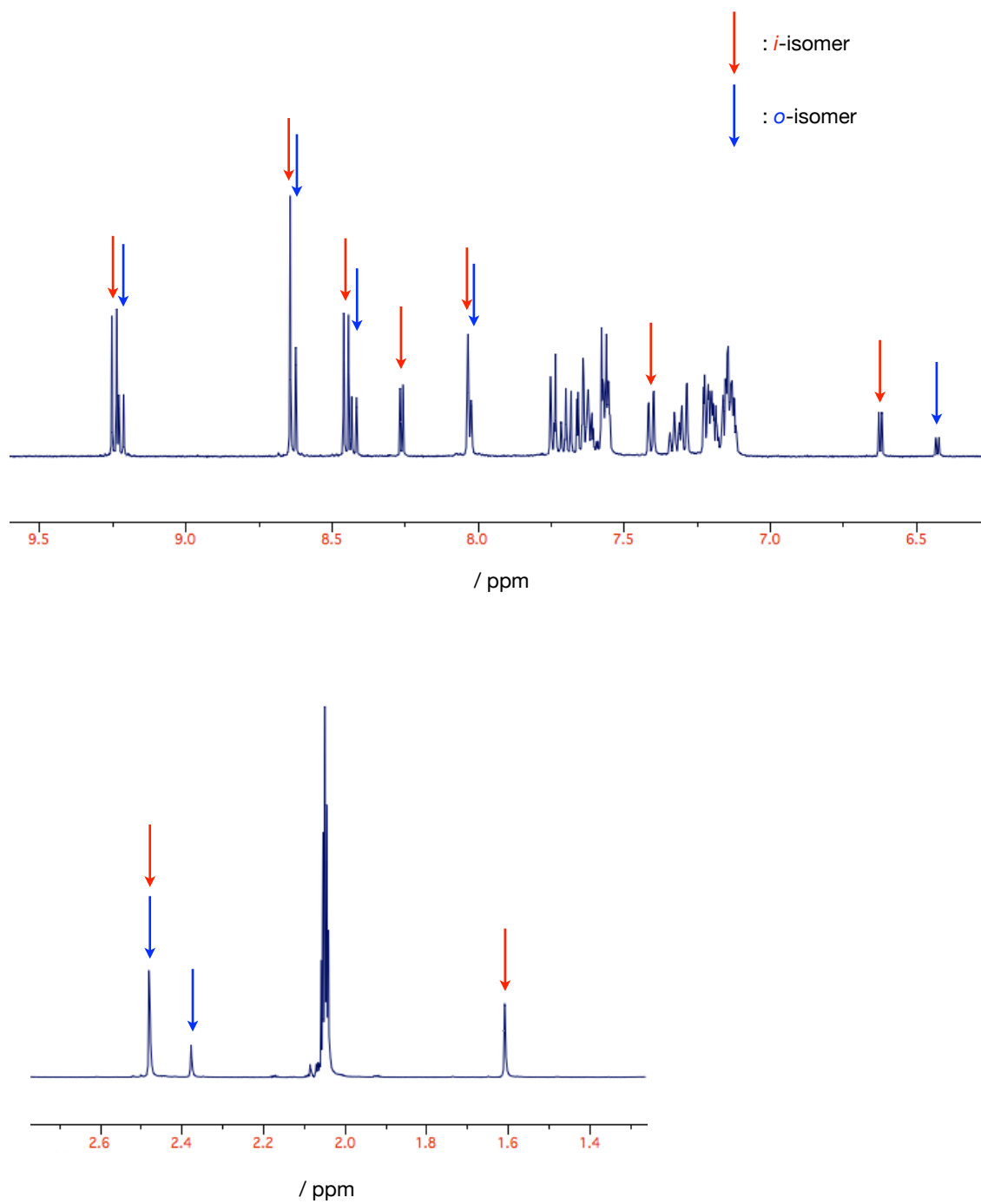


Fig. 2-4 ^1H NMR spectra of $1 \cdot \text{PF}_6$ in $\text{acetone-}d_6$ at room temperature.

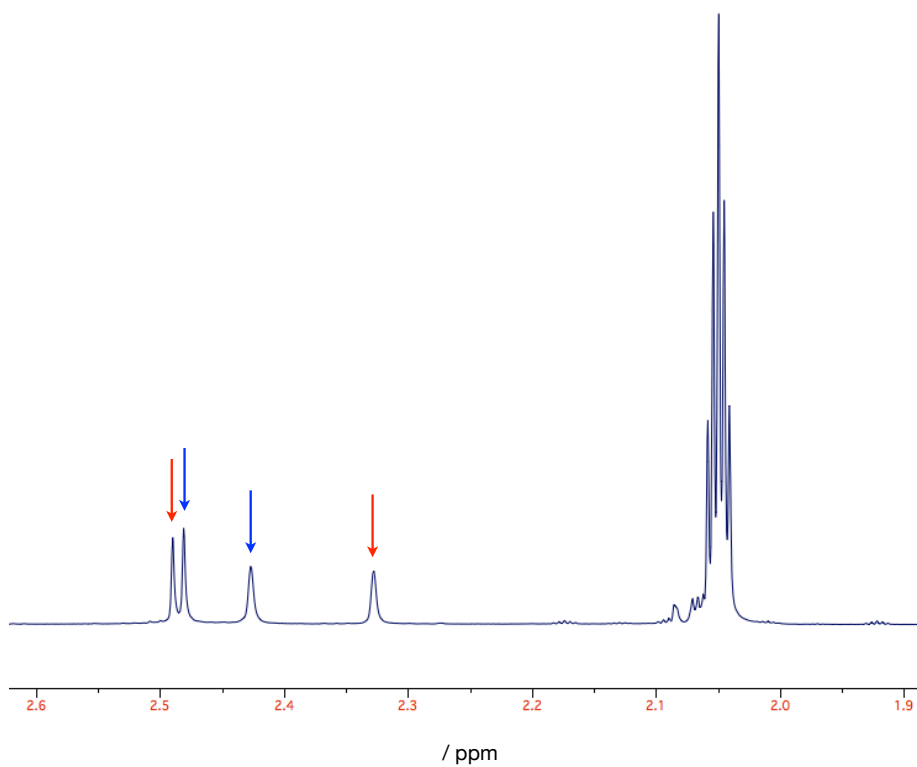
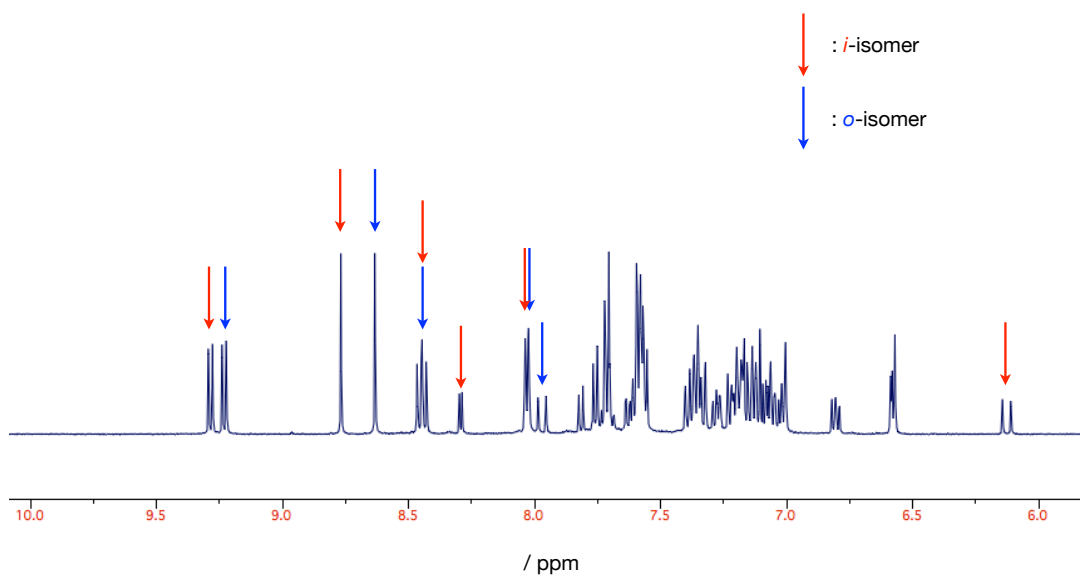


Fig. 2-5 ^1H NMR spectra of $2 \cdot \text{PF}_6$ in acetone- d_6 at room temperature.

2-3-3 Cyclic voltammetry in solution state

Cyclic voltammograms taken at room temperature in 0.1 M $n\text{Bu}_4\text{NPF}_6\text{-CH}_2\text{Cl}_2$ had two redox couples (Fig. 2-6). Based on the electrochemistry of Cu complexes,^{12,13} these signals were assigned to the redox reactions of the *o*- and *i*-isomer from the negative to the positive potential. The simulative analysis gave the rate constants, k_{io}^{I} and k_{io}^{II} , and the equilibrium constants, K_{io}^{I} and K_{io}^{II} (Table 2-2), which describe the *i* → *o* ring rotation at room temperature. The superscripts denote the copper's oxidation state. The results show that **1•PF₆** behaves identically to the complexes without a thioacetate moiety;⁹ therefore, elongation of the pyridine terminus has little impact on the rotational motion. On the other hand, the rotation rates of **2•PF₆** are slower than those of **1•PF₆**, although **2•PF₆** has the similar redox potentials to **1•PF₆**. This is also the consequence of the larger steric effect.

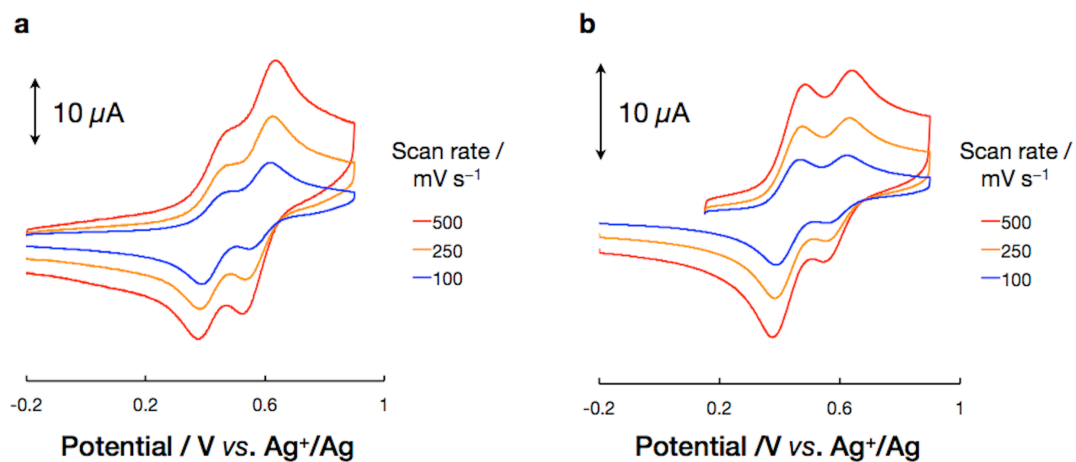


Fig. 2-6 Cyclic voltammetry in solution. a-b, Cyclic voltammograms of **1•PF₆** (a) and **2•PF₆** (b) in 0.1 M ⁿBu₄NPF₆-CH₂Cl₂ at room temperature.

Table 2-2 Fitting parameters of ring rotational process for **1•PF₆** and **2•PF₆**

Parameter	1•PF₆	2•PF₆
E_o / V	0.425	0.43
E_i / V	0.58	0.59
$K^I_{i \rightarrow o}$	0.47	1.3
$K^{II}_{i \rightarrow o}$	2.0×10^2	6.6×10^2
$ks_o / \text{cm s}^{-1[\text{a}]}$	0.4	0.4
$ks_i / \text{cm s}^{-1[\text{a}]}$	1	0.5
k^I_{io} / s^{-1}	0.8	0.4
$k^{II}_{io} / \text{s}^{-1}$	0.25	0.09
$\alpha_o^{[\text{b}]}$	0.5	0.5
$\alpha_i^{[\text{b}]}$	0.5	0.5
$R_u / \Omega^{[\text{c}]}$	1200	1500
$C_{dl} / \text{F}^{[\text{d}]}$	4.5×10^{-6}	4.5×10^{-6}
$D / \text{cm}^2 \text{s}^{-1[\text{e}]}$	1.0×10^{-5}	6.5×10^{-6}

[a] Electron transfer rate constant. [b] Transfer coefficient. [c] Resistance. [d] Capacitance. [e] Diffusion coefficient for all species.

2-3-4 XPS measurements on electrode surface

X-ray photoelectron spectra of 1-Au reveal peaks originating from Cu $2p_{1/2}$ and Cu $2p_{3/2}$, C 1s and N 1s were observed (Fig. 2-7a-c).

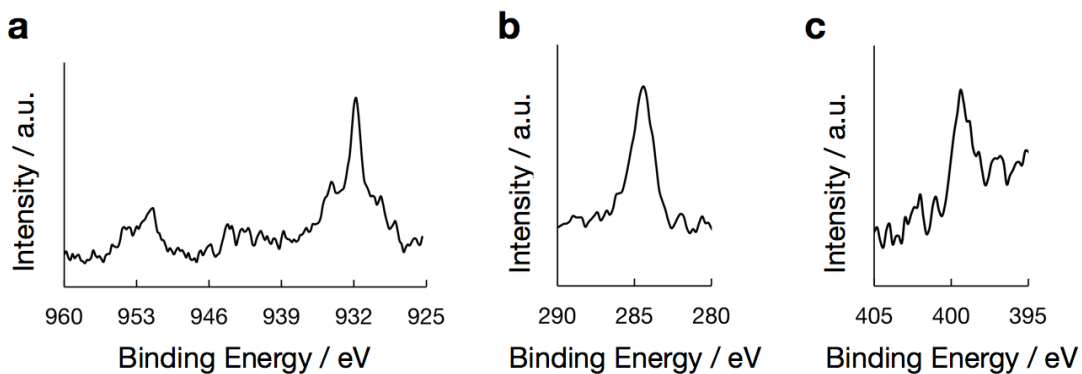


Fig. 2-7 (a-c) X-ray photoelectron spectra of **1-Au**. (a) Cu 2p, (b) C 1s, (c) N 1s. All spectra were calibrated according to the Au $4f_{7/2}$ peak at 83.8 eV.

2-3-5 Cyclic voltammetry on electrode surface

Two reversible redox waves, which were assigned to the two isomers according to the above discussion, appeared in the cyclic voltammograms of **1-Au** at the similar redox potentials to those of **1•PF₆** in solution, indicating that the conformation around the Cu center was retained after fixed on an Au surface (Fig. 2-8).

These overlapping redox waves were deconvoluted into the two Gaussian functions, as described in the following section, to give the peak currents and the ratio of the two isomers functionalized on the Au surface. In Fig. 2-9, the peak currents were plotted versus scan rate. The sums of the two isomers in the oxidation and reduction waves increase linearly with scan rate, which is consistent with the theoretical relation for redox species immobilized on electrode surfaces.¹⁴ Therefore, it was confirmed that the molecules were successfully immobilized on the Au surface. The same discussion is possible for the immobilization of **2-Au** (Figs. 2-10, 2-11). The differences between **1-Au** and **2-Au** are described more in detail in the following sections.

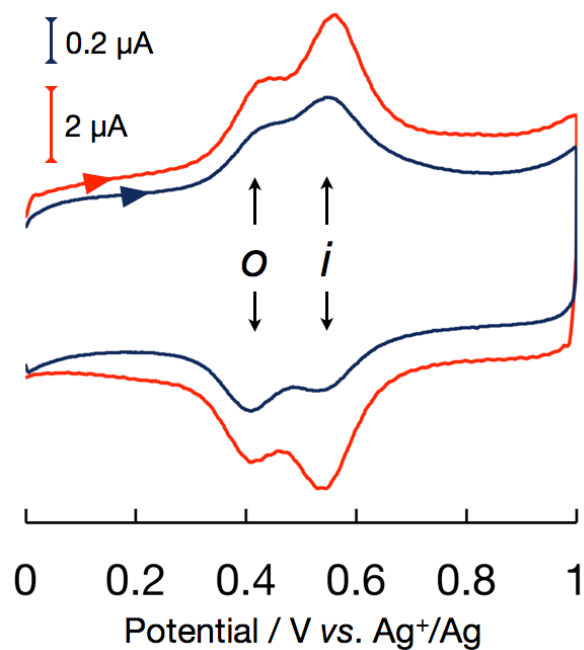


Fig. 2-8 Cyclic voltammograms of **1-Au** at room temperature in 1 M $t\text{Bu}_4\text{NPF}_6\text{-CH}_2\text{Cl}_2$. Scan rate: 1 V s^{-1} (red line) and 0.1 V s^{-1} (blue line).

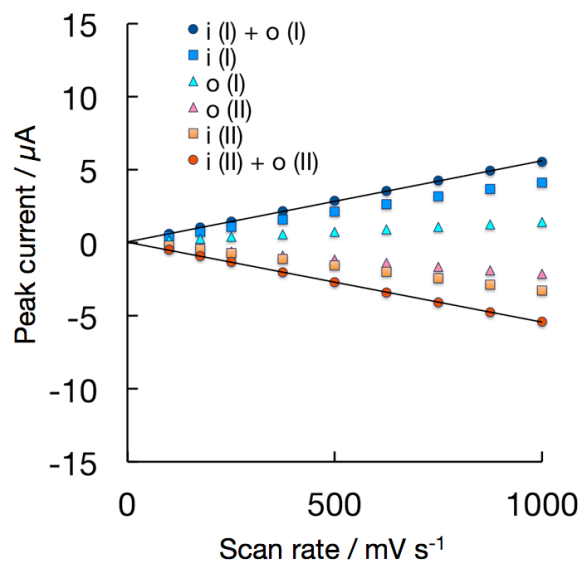


Fig. 2-9 Plots of peak currents versus scan rate for **1-Au**. The sums of peak currents of the two isomers have a linear dependence on scan rate for both the oxidation and reduction waves.

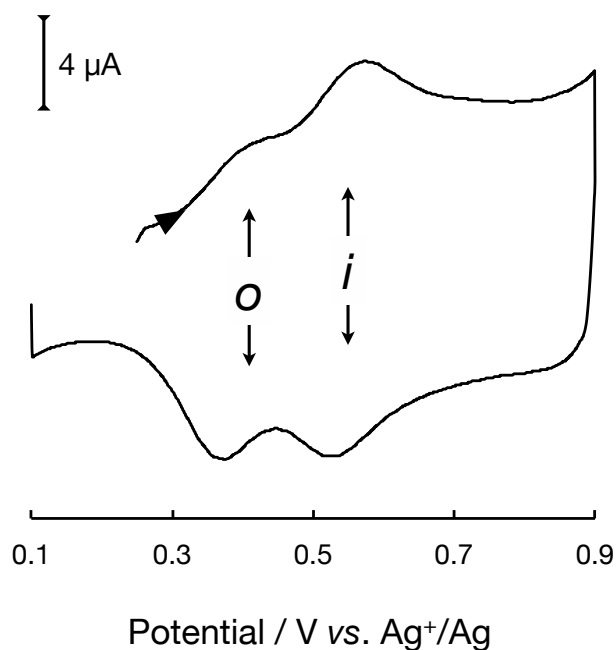


Fig. 2-10 Cyclic voltammograms of **2-Au** at room temperature in 1 M $n\text{Bu}_4\text{NPF}_6\text{-CH}_2\text{Cl}_2$. Scan rate: 1 V s^{-1} .

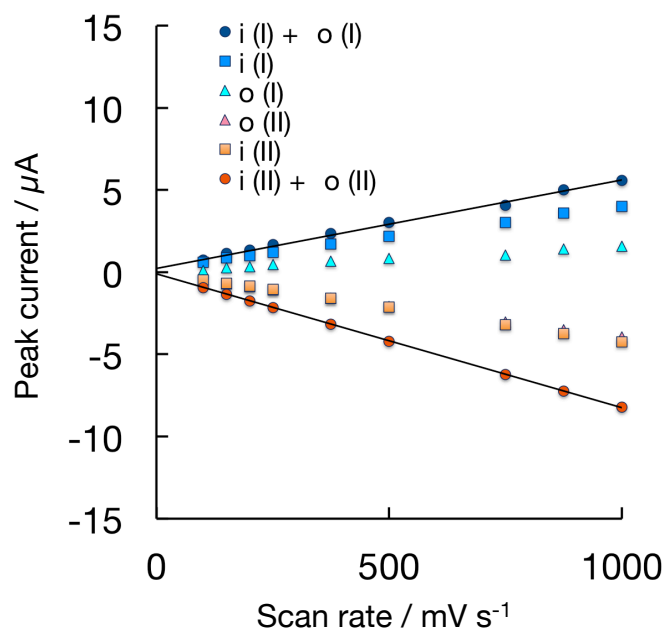


Fig. 2-11 Plots of peak currents versus scan rate for **2-Au**. The sums of peak currents of the two isomers have a linear dependence on scan rate for both the oxidation and reduction waves.

2-3-6 Simulative analysis on rotational behavior

Here the voltammograms of **1-Au** are taken as examples for the description of simulative analysis on cyclic voltammograms to obtain the thermodynamic and kinetic parameters. However, the same discussion can be applied to the case of **2-Au**.

Two overlapped redox signals were simulated with Gaussian functions according to the theory that current signals of species immobilized on electrodes are symmetrical, which is unlike signals of dissolved ones whose signals are desymmetrized due to diffusion. The central value and surface integral of each function correspond to the peak potential and amount of charge, respectively.

When molecules are oxidized, the rate constants change from their earlier values (Cu(I)) to the new values (Cu(II)) (Fig. 2-12). Right after oxidation, the system relaxes into the Cu(II) equilibrium, which are written by

$$k_{io}[i]_{\text{eq}} = k_{oi}[o]_{\text{eq}}$$

where k_{io} and k_{oi} are the forward and reverse rate constants, respectively (s^{-1}). The concentration of *i*- and *o*-isomers at the equilibrium state are $[i]_{\text{eq}}$ and $[o]_{\text{eq}}$, respectively.

The deviation of the concentration from the equilibrium value of Cu(II) is denoted as x . The concentration of *i*- and *o*-isomers, $[i]$ and $[o]$, can be expressed as follows:

$$[i] = x + [i]_{\text{eq}}, [o] = [o]_{\text{eq}} - x.$$

Therefore, the change of $[i]$ is written as follows:

$$\frac{d[i]}{dt} = -k_{io}([i]_{\text{eq}} + x) + k_{oi}([o]_{\text{eq}} - x) = -(k_{io} + k_{oi})x$$

Using the relation of $d[i]/dt = dx/dt$,

$$\ln x = -(k_{io} + k_{oi})t + \ln x_0$$

Hence, log plot of x is inversely proportional to time as shown in Fig. 2-14. The slope of log attenuation equals to the sum of rate constants in both directions. Because equilibrium constants ($K = k_{io}/k_{oi} = [o]_{\text{eq}}/[i]_{\text{eq}}$) can be calculated experimentally as follows, each rate constant is given. The time of Cu(II) (t) was estimated from the following equation including the peak potentials of the oxidation of *i*-isomer ($E_{p,i}^{\text{ox}}$), reduction of *o*- ($E_{p,o}^{\text{red}}$), and *i*-isomer ($E_{p,i}^{\text{red}}$) for a given scan rate, ν , and vertex potential, E_{λ} (Fig. 2-13a), respectively.

$$t = \left(2E_{\lambda} - E_{p,i}^{\text{ox}} - \frac{(E_{p,o}^{\text{red}} + E_{p,i}^{\text{red}})}{2} \right) / \nu$$

The baseline of the voltammograms (Fig. 2-13b), deconvolution of the redox waves (Figs. 2-13c and 2-13e) and the ratios of isomers in the redox waves versus scan rates (Figs. 2-13d and 2-13f) give the parameters for the equations for estimation of k_{io} and k_{oi} .

The equilibrium constants of Cu(I) could be calculated from deconvoluted oxidation wave on fast scan (1 V s^{-1}). The relationship between obtained equilibrium constant and redox potential is expressed as

$$RT \ln \frac{K^{\text{II}}}{K^{\text{I}}} = nF(E_i - E_o)$$

Therefore, calculated equilibrium constant in the Cu(I) state and two redox potentials of *i*-isomer and *o*-isomer derive the isomer equilibrium constant in the Cu(II) state.

The analysis described above is based on the premise that the ratio of isomers remains unchanged during redox processes. This is supported by the plot of ratios in Fig. 2-13d. It should be noted that significant decrease of inversion rate on surface allows this kind of analysis.

The description so far results in k_{io}^{II} , K_{io}^{I} and K_{io}^{II} . However, the same analysis cannot be simply applied to the first reduction waves and second oxidation waves for the calculation of k_{io}^{I} because the ratio of isomers in the first reduction wave varies with scan rate. In order to examine the Cu(I) rotation rate by monitoring the relaxation from non-equilibrium to equilibrium, preceding electrolysis was employed to establish equilibrium in the Cu(II) state. When the initial potential was held for 60 s at more positive potential than both isomer oxidation peak potentials, all molecules present were oxidized to the Cu(II) state (Fig. 2-14a). After preceding electrolysis, the system reached the equilibrium of Cu(II). The dependency of cyclic voltammograms on the scan rate reflects the changes in molar ratio (Fig. 2-14b). The constant ratio in the Cu(II) state ($o : i = 10 : 0$) was confirmed by deconvolution of reduction waves which gives the ratios of isomers in reduction waves versus scan rate. (Fig. 2-14c). The ratio of the anodic waves depends on the scan rate (Fig. 2-14d), because the isomer ratio in Cu(I) state is changed from a nonequilibrium state ($o : i = 10 : 0$) to the equilibrium state ($o : i = 2 : 8$). The analysis with a help of equations mentioned above gave the rate constants in the Cu(I) state, as shown in Fig. 2-15 and Table 2-3.

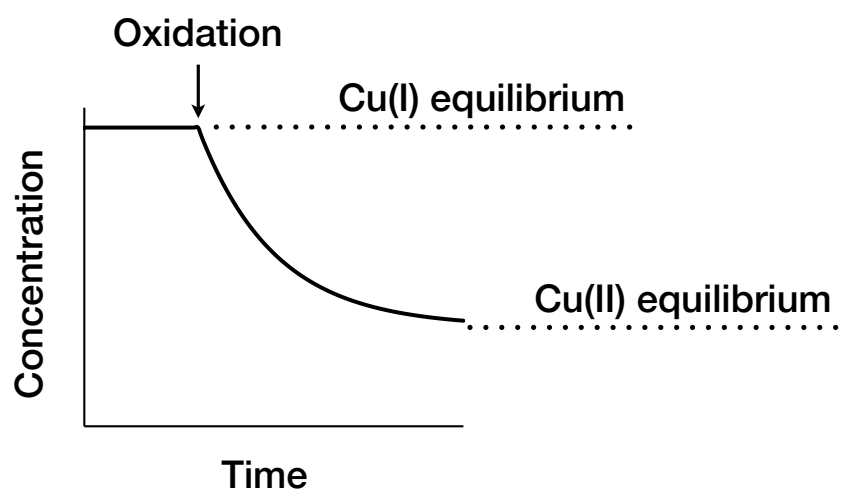


Fig. 2-12 Schematic of changes in concentration of isomers after oxidation.

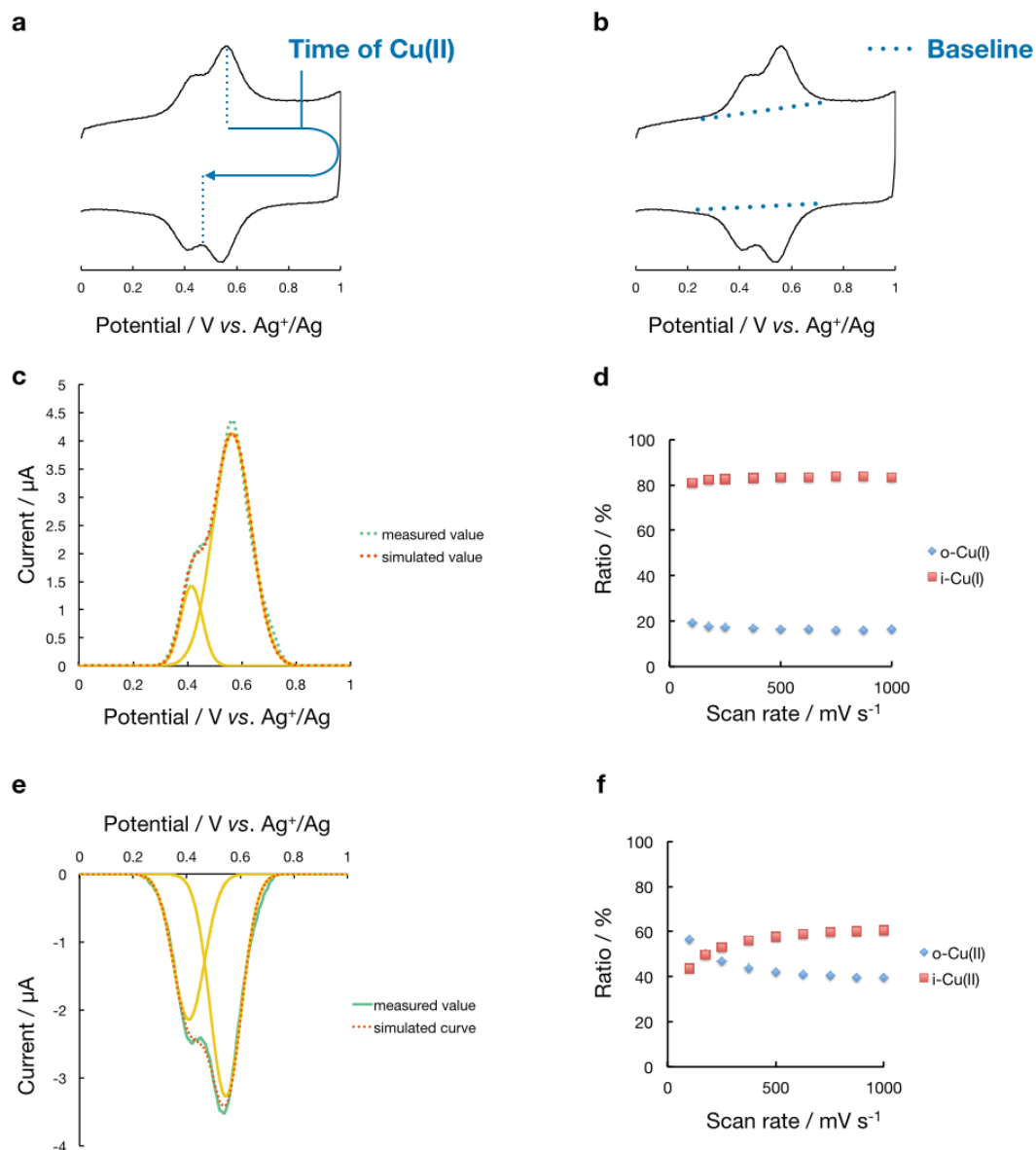


Fig. 2-13 Kinetic analysis of cyclic voltammograms to calculate the rotation rate of Cu(II) of **1-Au**. (a) Time of Cu(II) was estimated from both the scan rate and the potential region; an oxidation potential of *i*-isomer and a mean value of two reduction potentials. (b) Baselines set to correct the gradient of background. (c) Deconvolution of the oxidation wave (scan rate = 1 V s^{-1}). (d) Ratios of isomers in oxidation waves versus scan rates. The ratios (*o* : *i* = 2 : 8) were not dependent on the scan rates in the time scale of potential sweep. (e) Deconvolution of the reduction wave (scan rate = 1 V s^{-1}). (f) Ratios of isomers in reduction waves versus scan rates.

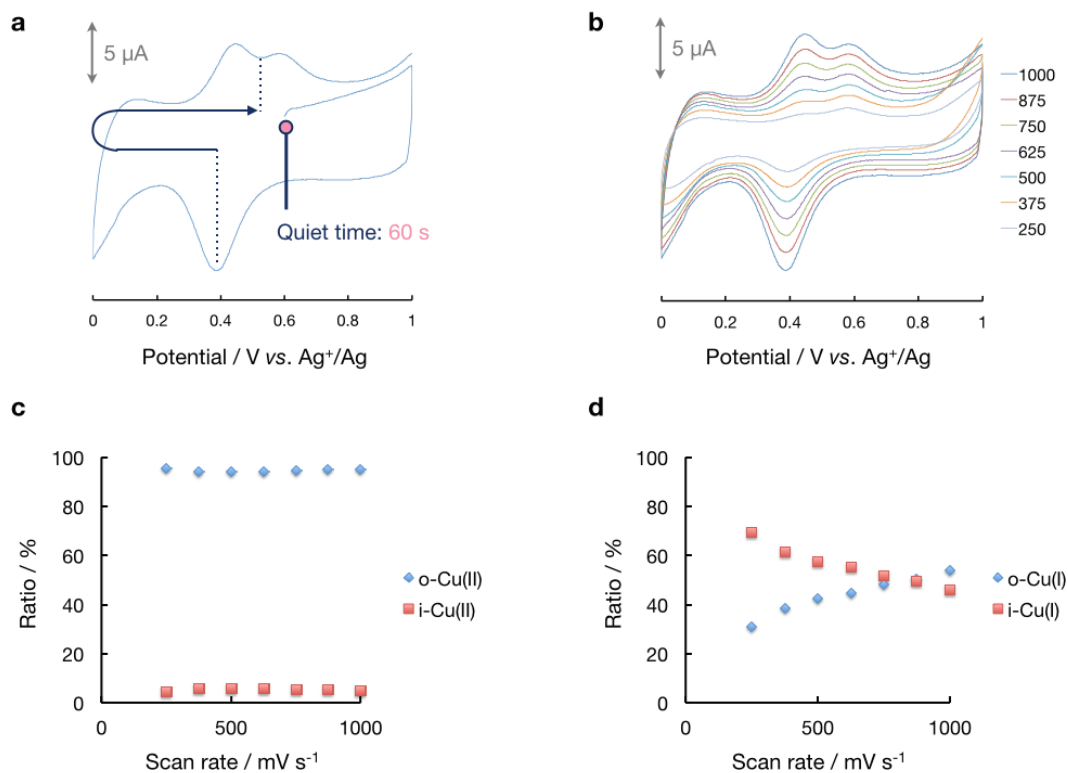


Fig. 2-14 Kinetic analysis of cyclic voltammograms to calculate the rotation rate of Cu(I) of **1-Au**. (a) Cyclic voltammograms after the preceding electrolysis. (b) The dependency of cyclic voltammograms on the scan rate. (c) The ratios of isomers in reduction waves versus scan rate. The ratio stays constant indicating the system reaches the equilibrium of the Cu(II) state. (d) The ratios of isomers in oxidation waves versus the scan rate.

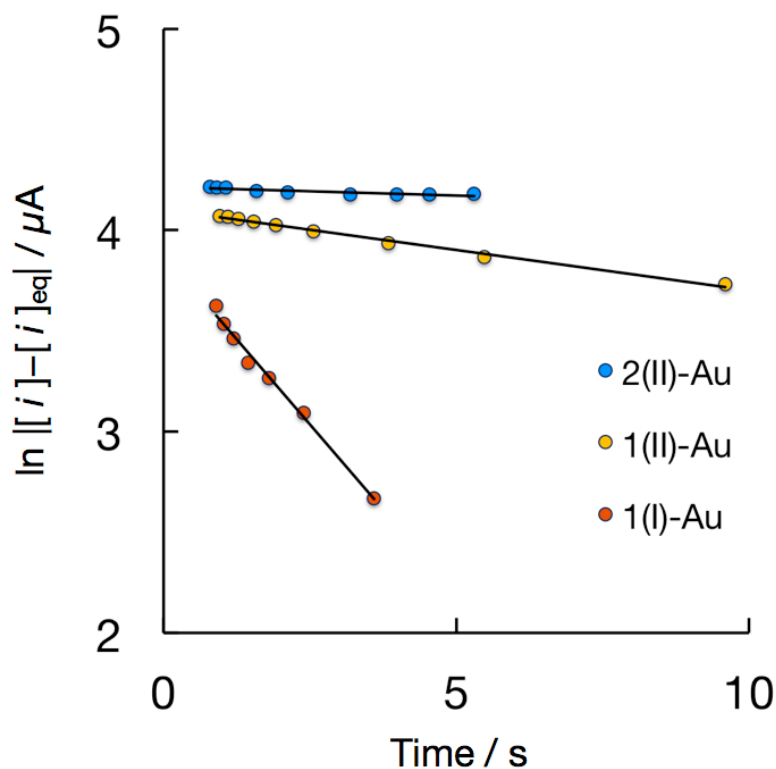


Fig. 2-15 Plots of $\ln |[i]-[i]_{\text{eq}}|$ vs. time.

Table 2-3 Parameters for rotation dynamics obtained from simulated cyclic voltammograms of **1-Au**, **2-Au**, **1•PF₆**, and **2•PF₆**

	1-Au	2-Au	1•PF₆^[d] (CH ₂ Cl ₂)	2•PF₆^[d] (CH ₂ Cl ₂)
E_o / V	0.41	0.38	0.425	0.43
E_i / V	0.55	0.54	0.58	0.59
$k_{io}^I / \text{s}^{-1[\text{a}]}$	0.06	- ^[c]	0.8	0.4
$k_{io}^{II} / \text{s}^{-1[\text{a}]}$	0.04	0.009	0.3	0.1
K_{io}^I ^[b]	0.20	0.19	0.47	1.3
K_{io}^{II} ^[b]	5×10	1×10^2	2×10^2	7×10^2

[a] Rate constant for the $i\text{-Cu} \rightarrow o\text{-Cu}$ rotation. [b] Equilibrium constants for $i\text{-Cu} \rightarrow o\text{-Cu}$ rotation, set as $K_{io} = k_{io}/k_{oi}$. [c] Preceding electrolysis was not completed within a reasonable time due to slow rotation in the Cu(II) state. [d] Cyclic voltammetry was carried out in 0.1 M ⁿBu₄NPF₆-CH₂Cl₂.

2-3-7 Thermodynamics and kinetics of rotation on Au surface

The aforementioned thermodynamic and kinetic parameters are tabulated in Table 2-3. The thermodynamic parameters in the solution state are similar to those obtained for the complexes immobilized on the electrode surface. The values of K_{io}^I are 0.47 for **1•PF₆** in solution and 0.20 for **1-Au**, respectively, indicating that the bistability of the Cu(I) state is achieved in both systems. K_{io}^{II} is significantly larger than K_{io}^I owing to the destabilization of *i*-Cu(II) by the steric repulsion present between the anthryl and methyl groups of the square planar structure. Such behavior is common in a series of the copper(I)-pyrimidine complexes.⁸ In contrast to the thermodynamic parameters, the kinetic parameters are entirely different depending on whether the complexes are present on the electrode surface or in solution. The calculated *i* → *o* rate constant in the Cu(II) state reveals a drastic decrease of the rotation rate of the complex upon surface-immobilization on gold surface ($k_{io}^{II} = 0.04 \text{ s}^{-1}$), which was about one-tenth of that in solution ($k_{io}^{II} = 0.3 \text{ s}^{-1}$). The conversion rate constant in the Cu(I) state ($k_{io}^I = 0.06 \text{ s}^{-1}$) is almost one-tenth of that in solution ($k_{io}^I = 0.8 \text{ s}^{-1}$).

It should be noted that the changes in the voltammograms induced by applied voltage, as mentioned above, allow not only for the estimation of the rotational parameters of the complexes on the electrode surface, but also for symptomatic of redox-synchronized pyrimidine ring rotation at room temperature. In the forward scanning to positive potentials, the *o*-isomer is first oxidized with no change in the *i/o* ratio followed by oxidation of *i*-isomer. The oxidation then proceeds by *i* → *o* isomerization.

For comparison, the thermodynamics and kinetics of pyrimidine ring rotation of **2•PF₆** in solution and on an Au electrode surface (**2-Au**) are also considered. The k_{io}^{II} value of **2-Au** is about one-third of that of **1-Au** (Table 2-3), indicating slower isomerization that can be attributed to the larger steric effect associated with the bulkier rotational unit. It is worth noting that this steric effect is also observed in solution; i.e., the rotation of **2•PF₆** was three times slower than **1•PF₆**. Therefore, the slow rotation of **2-Au** arises from the structure of the rotor moiety itself. As a corollary to the deceleration, relaxation to the Cu(II) equilibrium state is less aggressive and thus, in contrast to **1-Au**, the non-equilibrium Cu(II) state could be interestingly trapped at room temperature. This comparison leads us to an important conclusion that the rotational behavior of this system can be tuned by increasing (or decreasing) the degree of steric

hindrance acting between a rotor and anthryl panels, as the trajectory of rotational motion can be expected.

2-3-8 Repeatability of redox-synchronized rotation

In cyclic voltammetry, the rotational isomerization was observed between oxidation and reduction. The repeatability was studied in repetitive redox cycles (Fig. 2-16). The slow scan rate of 50 mV/s was chosen since the long duration between oxidation and reduction makes the isomerization clear. As seen in Fig. 2-16a, this rotational behavior is consistently observed with repeated scanning, indicating that the ligand rotation beside the copper center occurs without elimination.

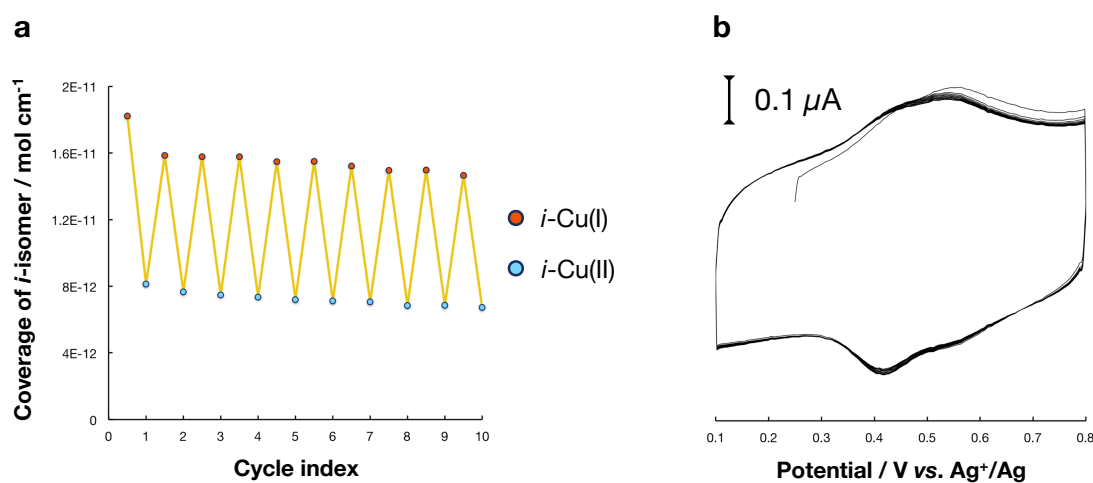


Fig. 2-16 Repeatability of rotational isomerization induced by redox reaction. a, A change in the surface coverage of *i*-isomer through repetitive redox processes. b, A cyclic voltammogram at a scan rate of 50 mV/s. The coverages of *i*-Cu(I) and *i*-Cu(II) were calculated from charge amounts of oxidation and reduction wave, respectively. **1-Au** was used for this experiment.

2-4 Conclusion

In this chapter, Cu-pyrimidine complexes were newly synthesized and immobilized on the Au surface. They showed redox-synchronized rotational isomerization in cyclic voltammetry and proved that this system can work even in the solid states. The fixation on Au surfaces enables the control of rotation just by an applied electrochemical potential from the electrode, as demonstrated in preceding electrolysis and repetitive redox cycles. This is contrary to the previous studies conducted in the solution states, where the rotation control can be accomplished by adding redox reagents into solutions. Furthermore, the application of this system to the Au surface also makes it possible to access to the individual molecules by scanning tunneling microscopy described in the next chapter. Considering the STM observation for long time scale compared with cyclic voltammetry, it should also be noted that the rotation rate drastically decreases by immobilization, which aids the STM experiment at room temperature.

2-5 References

- (1) Schmittel, M.; Michel, C.; Liu, S.-X.; Schildbach, D.; Fenske, D. *European Journal of Inorganic Chemistry* **2001**, *2001*, 1155–1166.
- (2) Kume, S.; Nomoto, K.; Kusamoto, T.; Nishihara, H. *J. Am. Chem. Soc* **2009**, *131*, 14198–14199.
- (3) Wu, J.; Chi, C.; Wang, X.; Li, J.; Zhao, X.; Wang, F. *Synthetic Communications* **2000**, *30*, 4293–4298.
- (4) Baba, D., Ono, Y., Electron transport material and organic electroluminescence element using same. PCT Int. Appl. WO 2012060374 A1 (2012).
- (5) Altomare, A.; Cascarano, G.; Giacobozzo, C.; Guagliardi, A.; Burla, M. C.; Polidori, G. T.; Camalli, M. *J Appl Crystallogr* **1994**, *27*, 435–436.
- (6) Sheldrick, G. M. *Acta Crystallogr., A, Found. Crystallogr.* **2008**, *64*, 112–122.
- (7) Farrugia, L. J. *J Appl Crystallogr* **1999**, *32*, 837–838.
- (8) Nomoto, K.; Kume, S.; Nishihara, H. *J. Am. Chem. Soc* **2009**, *131*, 3830–3831.
- (9) Nishikawa, M.; Kume, S.; Nishihara, H. *Phys. Chem. Chem. Phys.* **2013**.
- (10) Kume, S.; Nishihara, H. *Chemical Communications* **2011**, *47*, 415–417.
- (11) Kume, S.; Nishihara, H. *Dalton Trans* **2011**, *40*, 2299–2305.
- (12) Federlin, P.; Kern, J. M.; Rastegar, A.; Dietrichbuecker, C.; Marnot, P. A.; Sauvage, J. P. *New J. Chem.* **1990**, *14*, 9–12.
- (13) Kume, S.; Kurihara, M.; Nishihara, H. *Inorg. Chem.* **2003**, *42*, 2194–2196.
- (14) Bard, A. J.; Faulkner, L. R. *Electrochemical Methods: Fundamentals and Applications*; 2nd ed.; John Wiley & Sons: New York, 2001.

Chapter 3

STM Observation of Rotational Motion

3-1 Introduction

Electrochemical analysis revealed that this system could be functionalized on the Au surface in Chapter 2. The rotational motion is studied by STM in this chapter. It is noteworthy that STM can pick up the response of individual molecules while the redox waves in cyclic voltammograms are the integrated signals of all the molecules absorbed on the surface, and thus this is the demonstration to prove the function of this Cu-pyrimidine system as a single molecule machines.

The most distinguished feature of this system is the correlation between the electronic state and the structure. If a small degree of motion can be detected as the conductivity change, the same method would be adopted to other single molecule studies because it may overcome a critical issue that STM has a limit in its resolution at high temperature due to thermal drift of a swept tip with respect to the surface. Although some study focuses on the observation of single molecules at room temperature, either of molecular size or degree of structural change must be enlarged to enable observation. That is one point; however, it should be noted that to enlarge molecule or molecular motion results in the decrease of the number of molecular units on surface, which spoils an advantage of molecular-based devices: miniaturization of device size.

This chapter describes the preparation of the mixed SAM of **1** and 1-hexanethiol for the continuous monitoring of individual molecules. STM observation held on the mixed SAM suggested the conductivity changes assigned to the rotational isomerization. The origin of the conductivity changes was discussed in terms of the electronic states of the two isomers, and it was concluded that the conductivity change was derived from the change of the electron charge distributions of the frontier molecular orbitals of the two isomers. Moreover, an additional Cu complex **3** was synthesized with a bipyridine ligand, which has no altering nitrogen to coordinate to copper, to confirm that the conductivity change was derived from the charge distribution change associated with the rotation. LT-UHV STM measurement was also performed for the mixed-SAM of **1**, indicating the thermal suppression of the rotation dynamics.

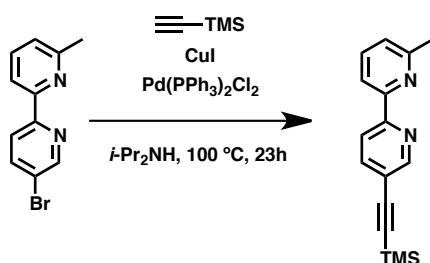
3-2 Experimental

3-2-1 Materials

5-bromo-6'-methyl-2,2'-bipyridine were prepared according to literature methods.¹ CH₂Cl₂ and THF were purified by Glass Contour Solvent Purification system (Nikko Hansen & Co., Ltd.). Other chemicals were used as purchased.

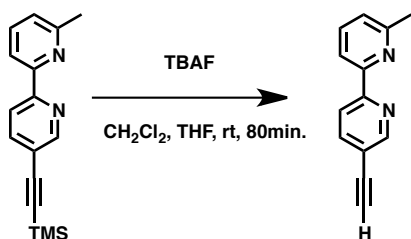
3-2-2 Synthesis

6'-methyl-5-((trimethylsilyl)ethynyl)-2,2'-bipyridine (**12**)



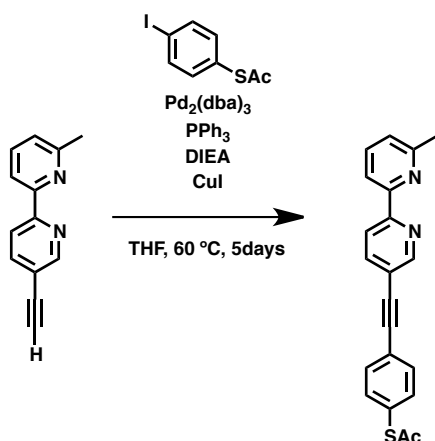
Under a nitrogen atmosphere, 5-bromo-6'-methyl-2,2'-bipyridine (1.42 g, 5.71 mmol), copper(I) iodide (142 mg, 0.744 mmol) and Pd(PPh₃)₂Cl₂ (364 mg, 0.518 mmol) were added to *i*-Pr₂NH (50 mL). To the solution, trimethylsilylacetylene (1.32 mL, 9.20 mmol) was added and stirred for 23 h at 100°C. The resulted black solution was filtered and washed with CH₂Cl₂. The filtrate was evaporated and the crude product was purified with alumina column chromatography eluted with ethyl acetate/hexane (1:1v/v) to give a yellow-white powder of **12**. Yield: 594 mg (39 %). ¹H NMR (500 MHz, CDCl₃) δ 8.72 (d, *J* = 2.1 Hz, 1H), 8.38 (d, *J* = 8.2 Hz, 1H), 8.18 (d, *J* = 7.8 Hz, 1H), 7.85 (dd, *J* = 8.2, 2.1 Hz, 1H), 7.70 (t, *J* = 7.7 Hz, 1H), 7.18 (d, *J* = 7.6 Hz, 1H), 2.63 (s, 3H), 0.28 (s, 9H).

5-ethynyl-6'-methyl-2,2'-bipyridine (**13**)



12 (594 mg, 2.23 mmol) and tetra-*n*-butylammonium fluoride (2.3 ml, 1M in THF) were stirred in CH₂Cl₂ for 80 min at room temperature. The solution was filtered, and the filtrate was evaporated. The crude product of **13** was purified with alumina column chromatography eluted with CH₂Cl₂. Yield: 433 mg (100 %). ¹H NMR (500 MHz, CDCl₃) δ 8.76 (d, *J* = 2.1 Hz, 1H), 8.41 (d, *J* = 8.2 Hz, 1H), 8.18 (d, *J* = 7.8 Hz, 1H), 7.89 (dd, *J* = 8.2, 2.1 Hz, 1H), 7.71 (t, *J* = 7.7 Hz, 1H), 7.19 (d, *J* = 7.6 Hz, 1H), 3.29 (s, 1H), 2.64 (s, 3H). MALDI-TOF-MS *m/z* 195.16 (calcd. for [M+H]⁺, 195.09).

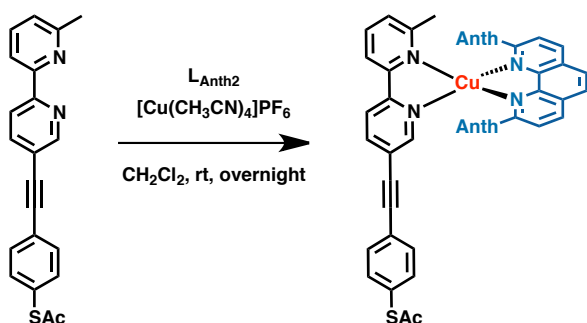
S-(4-((6'-methyl-[2,2'-bipyridin]-5-yl)ethynyl)phenyl) ethanethioate (**bpySAc**) (**14**)



Under a nitrogen atmosphere, *S*-acetyl-4-iodothiophenol (83.7 mg, 0.301 mmol), tris(dibenzylideneacetone)dipalladium (6.9 mg, 0.0075 mmol), triphenylphosphine (15 mg, 0.057 mmol), copper(I) iodide (4.8 mg, 0.025 mmol) were added to THF (15 ml). *i*-Pr₂NEt (0.26 ml, 1.5 mmol) and **13** (57.4 mg, 0.296 mmol) were added and the

reaction mixture was stirred for 5 days at 60°C. The solution was filtered, and the solvent was evaporated. A yellow-white solid of **14** was given by purification with silica column chromatography eluted with CH₂Cl₂. Yield: 76.4 mg (74 %). ¹H NMR (500 MHz, CDCl₃) δ 8.81 (d, *J* = 2.1 Hz, 1H), 8.44 (d, *J* = 8.2 Hz, 1H), 8.20 (d, *J* = 7.8 Hz, 1H), 7.93 (dd, *J* = 8.2, 2.1 Hz, 1H), 7.72 (t, *J* = 7.7 Hz, 1H), 7.60 (d, *J* = 8.2 Hz, 2H), 7.43 (d, *J* = 8.2 Hz, 2H), 7.19 (d, *J* = 7.6 Hz, 1H), 2.65 (s, 3H), 2.45 (s, 3H). MALDI-TOF-MS *m/z* 345.30 (calcd. for [M+H]⁺, 345.11).

[Cu(bpySAc)(L_{Anth2})]PF₆ (2·PF₆)



Under a nitrogen atmosphere, 2,9-bis(9-anthracenyl)-1,10-phenanthroline (L_{Anth2}, 29 mg, 54 μmol) and [Cu(CH₃CN)₄]PF₆ (20 mg, 54 μmol) were stirred for 40 min in dichloromethane. To the resulted orange clear solution, bpySAc (19 mg, 55 μmol) was added and the solution immediately changed to deep red. After filtration, diethyl ether was added to the filtrate to precipitate **2·PF₆** as a deep red solid. Yield: 46.6 mg (80 %). ¹H NMR (500 MHz, (CD₃)₂CO) δ 9.22 (d, *J* = 8.2 Hz, phen), 8.63 (s, phen), 8.41 (d, *J* = 8.2 Hz, phen), 8.04 (s, Anth), 7.72 (d, *J* = 8.4 Hz,), 7.62 (d, *J* = 8.3 Hz,), 7.58-7.55 (m), 7.40-7.39 (m), 7.30-7.28 (m), 7.20-7.13 (m), 2.45 (s), 1.61 (s). ESI-TOF-MS *m/z* 939.2206 (calcd. for [M-PF₆]⁺, 939.2219).

3-2-3 Experimental apparatus

STM measurements were performed using a Agilent 5500 (Agilent) under ambient conditions and with a modified UHV-STM system (UNISOKU) with a base pressure below 3.0×10^{-8} Pa at 68 K. The STM tips were prepared by electrochemically etching a tungsten wire (0.25 mm ϕ) in 1 M KOH.

3-3 Results and Discussion

3-3-1 Control of surface density

After 15 min immersion of an Au/mica substrate into a 0.1 mM dichloromethane solution of **1**, the complexes were uniformly immobilized on the gold electrodes as shown in an STM image of Fig. 3-2a. The sparse immobilization was required for STM experiment in terms of the continuous monitoring of a single molecule. To fill this requirement, a mixed SAM of **1** and 1-hexanethiol was prepared by established insertion methods.²⁻⁴ In these procedures, the target molecules were inserted into a preliminary-prepared alkanethiol SAM as depicted in Fig. 3-1. Fig. 3-2b is an STM image of 1-hexanethiol SAM. The black defects are etch pits generated with reconstruction of Au surface modified with hexanethiols.^{5,6} Fig. 3-2c is an STM image of a mixed SAM, where the bright spots in the Fig. 3-2a are successfully dispersed in the matrix of hexanethiol. These spots are assigned to the molecules **1**, because all the molecules in Fig. 3-2c appear uniform in size, which is also consistent with the sizes in Fig. 3-2a.

The sizes of spots in the STM images (a circle with 2 nm diameter) are larger than the physical size expected from the van der Waals radius of a molecule **1** (~1 nm diameter). This difference is due to the variation in the curvature of the STM tips. In STM measurement, the apparent size of a molecule inevitably appears larger than its actual size because the round tip starts to detect a molecule before it comes just above the molecule.

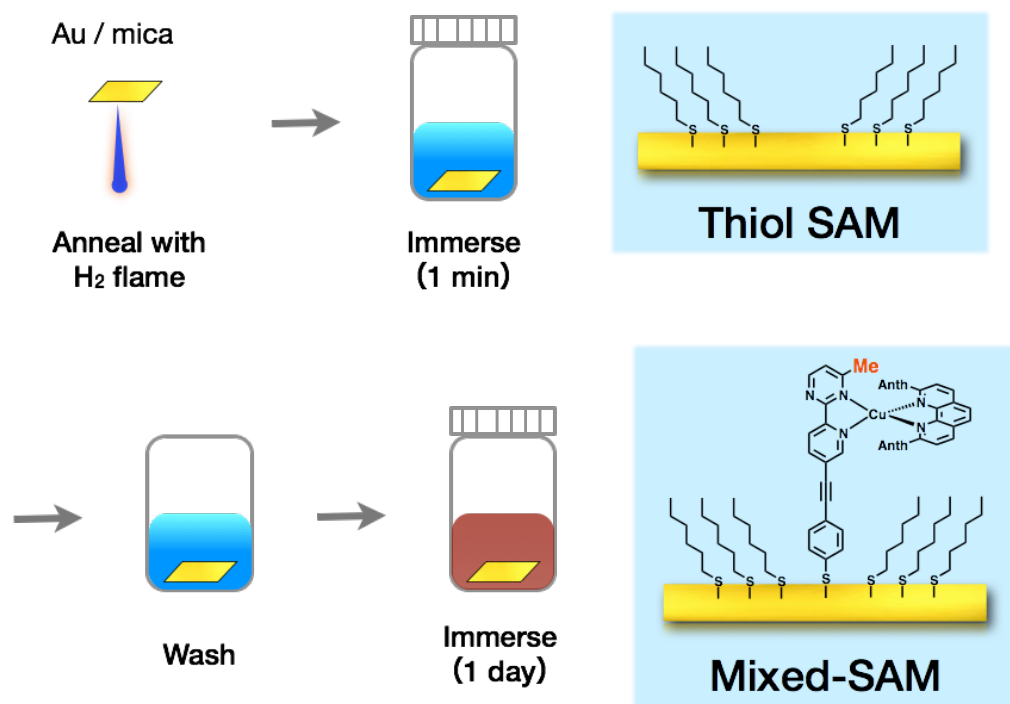


Fig. 3-1 Schematic of preparation of a mixed-SAM.

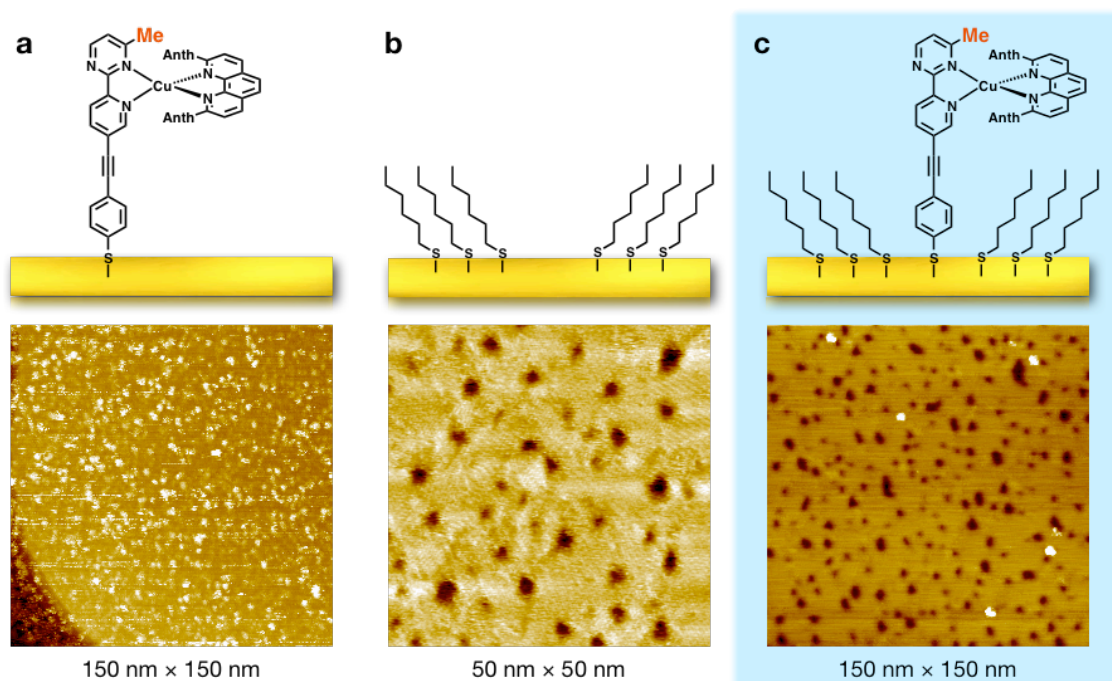


Fig. 3-2 STM images of SAMs of **1** (a), 1-hexanethiol (b) and a mixed-SAM (c). $V_s = 1.1$ V, $I_t = 0.1$ nA.

3-3-2 STM observation under ambient condition

STM experiments were first performed on the mixed SAM of **1** and 1-hexanethiol under ambient condition. The molecules on Au(111) were continuously monitored for more than one hour and data were collected. Fig. 3-3 shows successive shots of **1**, indicating the blinking behavior; a bright spot became dark and later turned back. As STM experiment was conducted in constant height mode, the tip was swept on the surface to keep the detected current constant (Fig. 3-4), and thus the brightness here indicates the apparent height; the brighter a molecule is, the higher. Therefore the blinking of molecules can be regarded as the change of conductivity.

The apparent height of the molecule **1** was defined as the height difference between **1** and 1-hexanethiol. The apparent height of 1-hexanethiol was defined as the averaged height of a selected area ($\sim 10 \text{ nm} \times 10 \text{ nm}$ size) on a 1-hexanethiol matrix, which is near a molecule and not inclusive of any etch pits. Then the value was subtracted from the height of the molecule that was set as the maximum apparent height in the spot.

The apparent height change of a molecule is shown in Fig. 3-5. It suggests that the molecule switches between the two states. The aggregated apparent height data (Fig. 3-6) were made from approximately 10 samples in 60 frames. Least square fitting of this histogram revealed two Gaussian components with apparent heights of 0.50 nm and 0.72 nm. The area ratio of the two conformations is 7 : 3, which seems consistent with the equilibrium ratio of **1** ($i : o = 8 : 2$, see chapter 2). The above discussions suggest molecules switch between the two conductivity states, which can be assigned to the two isomers.

The slowed rotation of the immobilized complexes allowed the observation of individual molecules by STM; given the scan rate (4.86 line/s), the size of a molecule (a circle with a radius of 1 nm) and resolution (256 points/line), the time taken by the STM tip to pass through each molecule is estimated to be $\sim 0.04 \text{ s}$, which is less than the period between each molecule's changes between i - and o -states.

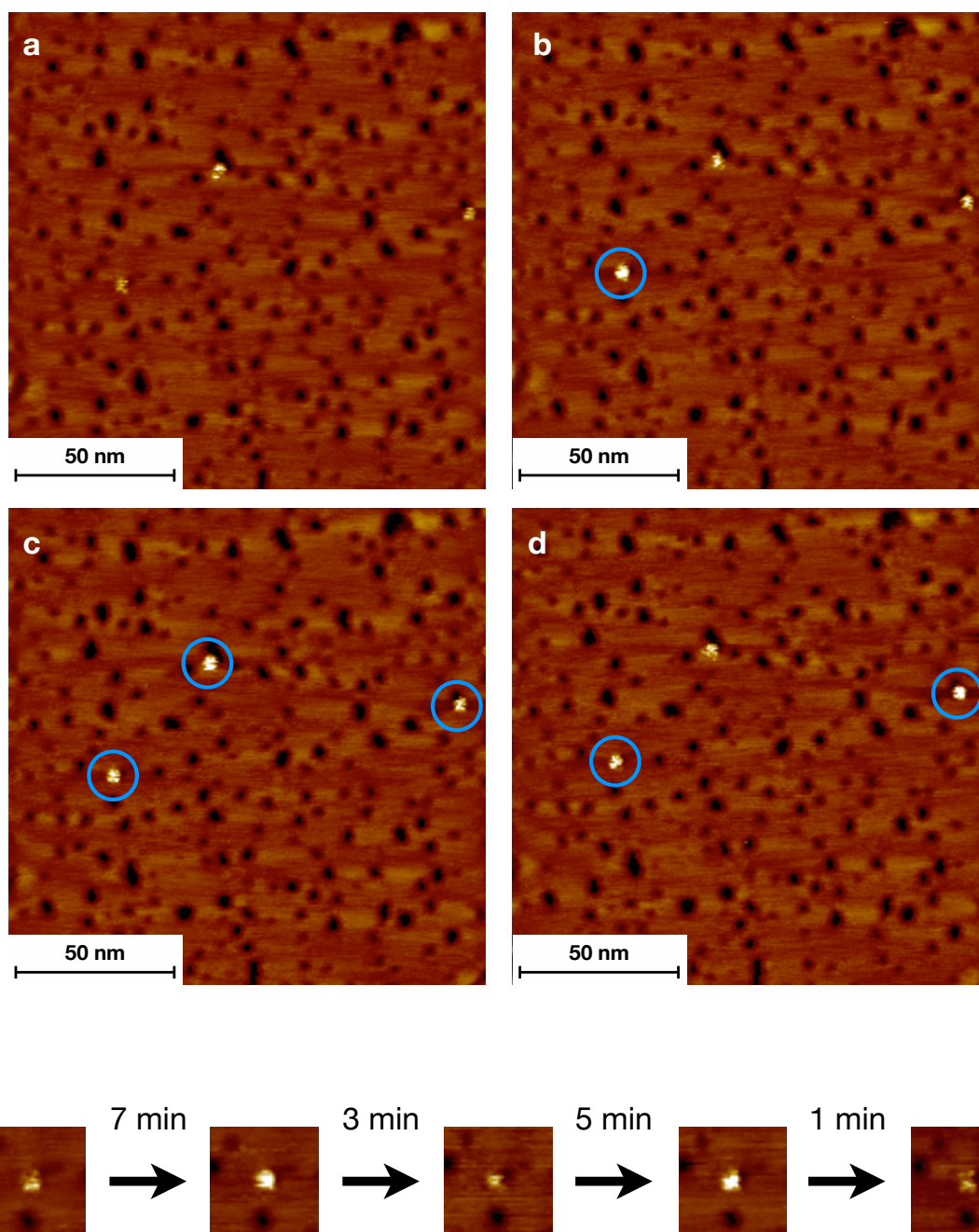


Fig. 3-3 (a-d) Successive STM topographic images of the mixed SAM of **1**. Blue circles indicate spots with higher apparent heights. Scan rate: 53 s/frame. $V_s = 1.1$ V, $I_t = 0.1$ nA. (e) Topographic changes of **1** under the ambient condition with the time intervals.

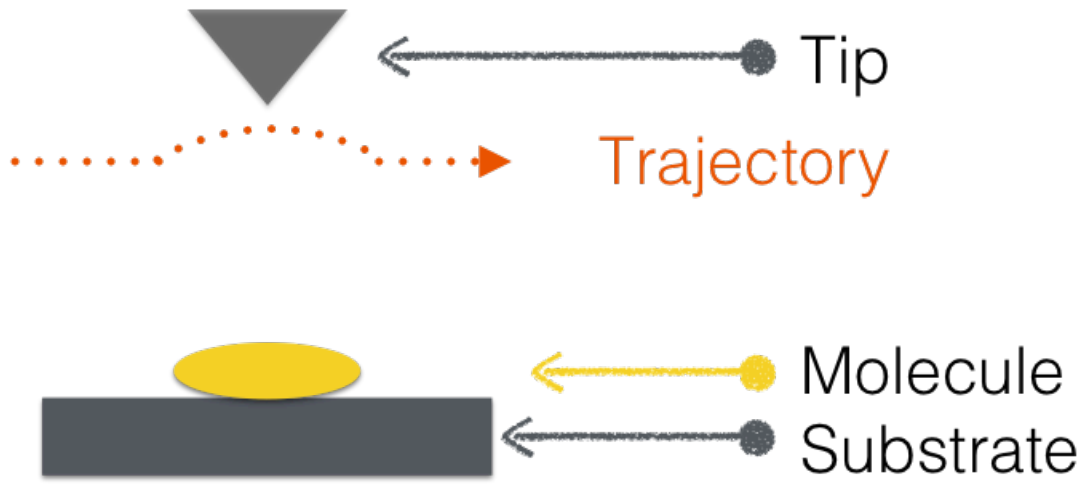


Fig. 3-4 Schematic of STM experiment performed in constant height mode.

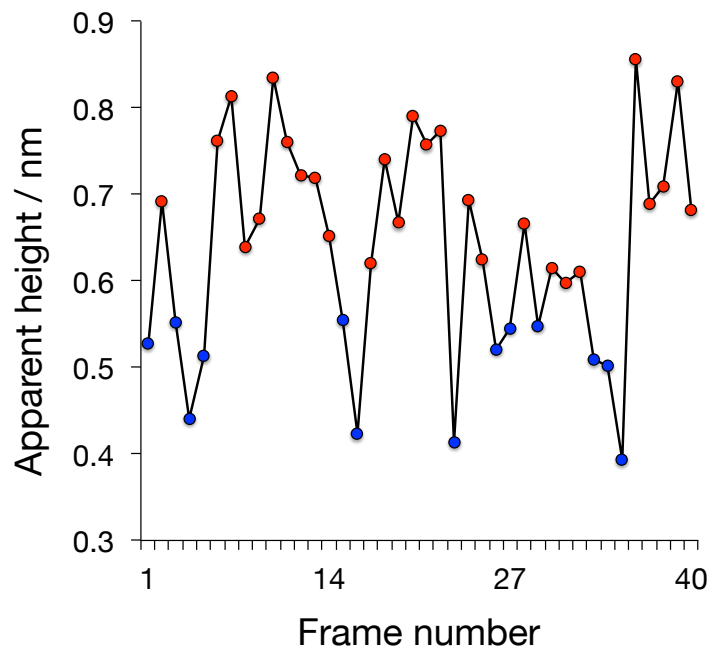


Fig. 3-5 Plot of apparent height vs. frame number for a selected molecule.

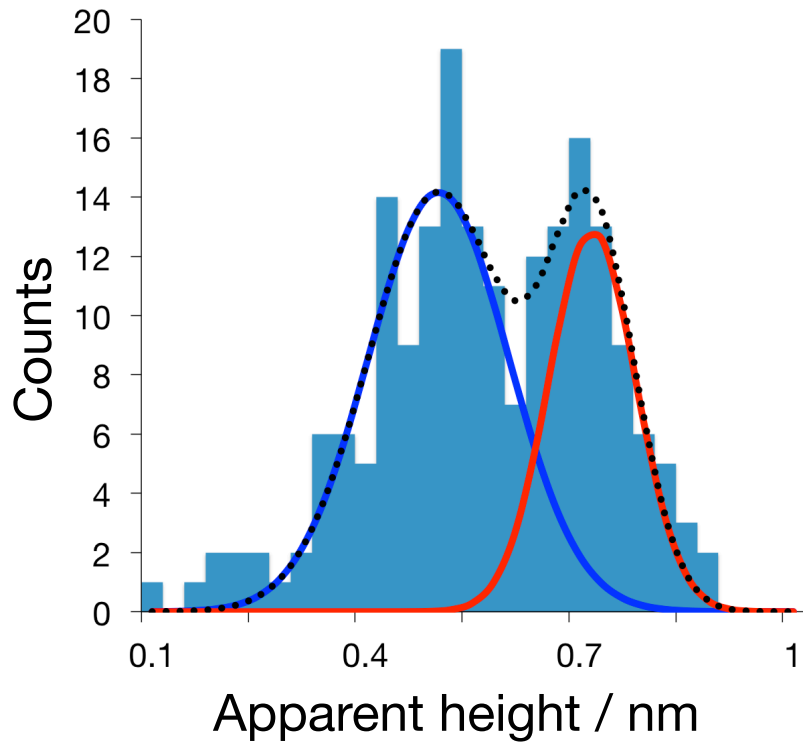


Fig. 3-6 Apparent height counts aggregated over 60 frames.

Table 3-1 Parameters of two components of the histogram in Fig. 3-6

	1	2
Median	0.50 nm	0.72 nm
Area ratio	74 %	26 %

3-3-3 Origin of blinking behavior

The assignment to two rotational isomers can be explained in terms of their electronic structures, where the *i*-isomer is topographically lower than the *o*-isomer. The apparent height change corresponds to a change in tunneling current since STM imaging was performed in constant current mode.

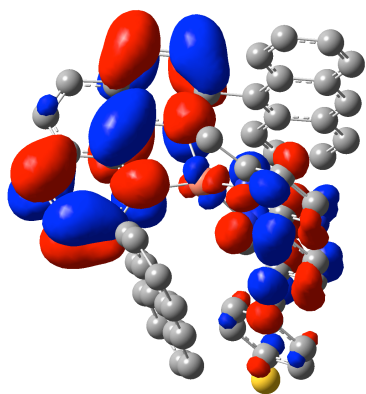
The molecular structures of the two isomers were optimized using density functional theory (DFT) at the BP86 level of theory. LANL2DZ basis set was used for Cu atom and the 6-31G(d) basis set for the other atoms. The contour surfaces and energy levels of the HOMOs and LUMOs are shown in Fig. 3-7. The HOMOs are to some extent localized on the Cu centers and anthryl groups for the two isomers, which is consistent with the Cu-centered redox reaction observed in the electrochemical measurements in Chapter 2. The LUMO of the *o*-isomer delocalizes onto the entire pyridylpyrimidine ligand. On the other hand, the LUMO of the *i*-isomer is on the phenanthroline group as well as the pyridylpyrimidine moiety and it does not distribute on the sulfur terminus of the pyridylpyrimidine ligand. Since the positive potential is applied to sample surface, electrons tunnel quantum mechanically through the LUMO of the sample (Fig. 3-8). Deduced from the electron density distribution, the LUMO of the *o*-isomer is expected to form electronic coupling with substrate via the terminal sulfur atom stronger than that of the *i*-isomer. In this situation, the *o*-isomer can mediate the tunneling current flowing from the tip to the substrate more efficiently, giving rise to a higher apparent height. The difference in the electron density distributions of the LUMOs is presumably derived from the different coordination geometries of the phenanthroline ligands of the two isomers; the π^* orbital of the phenanthroline of the *i*-isomer is lowered in energy by the steric effect of the methyl group to increase its contribution to the LUMO, which consists mostly of the orbital of the pyridylpyrimidine ligand in the *o*-isomer.

Among the observed protrusions, some disappeared in the thiol SAM but later returned. This behavior occurred independently of the switching discussed above and was thus attributed to changes of hybridization.⁷⁻⁹

Figure 3-9 shows the STM images with the corresponding isomers. As discussed above, the *o*-isomer is topographically higher than the *i*-isomer in this measurement condition.

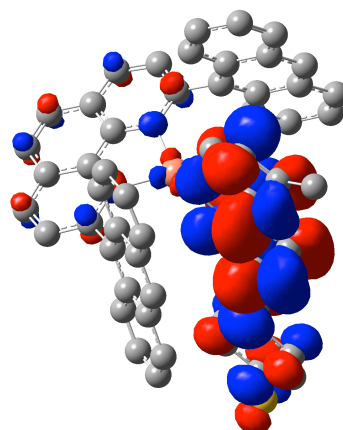
LUMO (*i*-isomer)

-5.13 eV



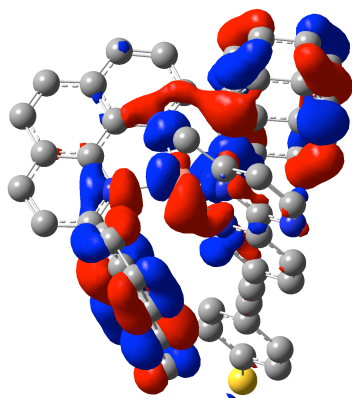
LUMO (*o*-isomer)

-5.09 eV



HOMO (*i*-isomer)

-6.81 eV



HOMO (*o*-isomer)

-6.79 eV

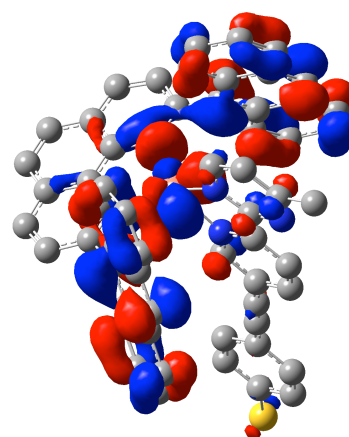


Fig. 3-7 Contour plots of the calculated frontier molecular orbitals of the two isomers. The structures were optimized using DFT (BP86/LANL2DZ for Cu, /6-31G(d) for the other atoms).

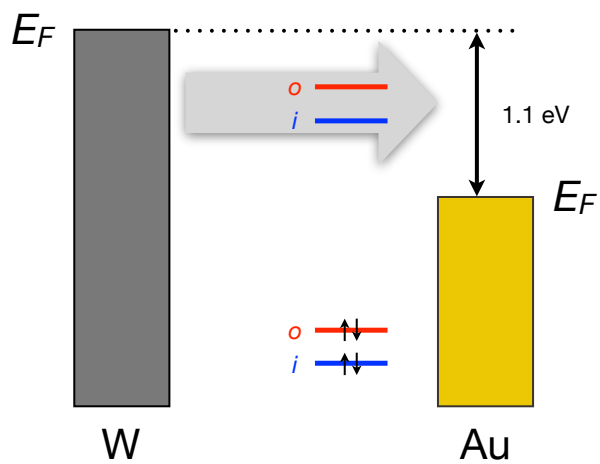


Fig. 3-8 Schematic diagram of resonant tunneling through the unoccupied orbitals.

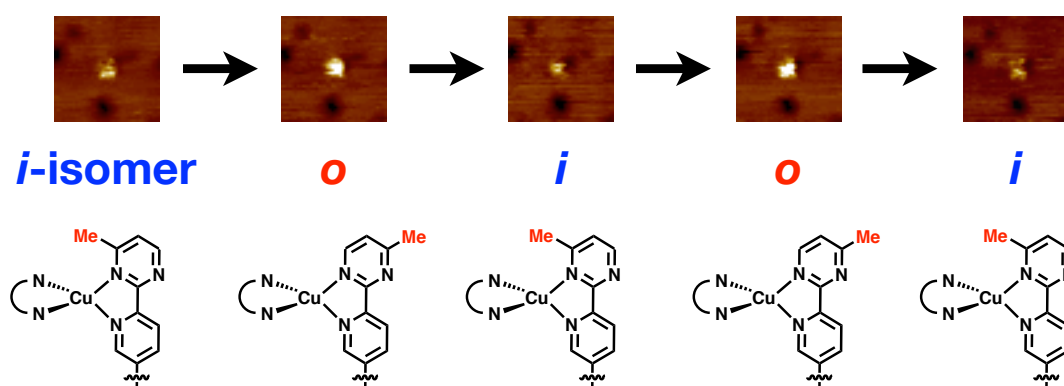


Fig. 3-9 STM images and corresponding isomers.

3-3-4 Comparison with Cu-bipyridine complex

To confirm further that the blinking images were certainly induced by rotational isomerization, STM images were taken for the mixed SAM of **3**•PF₆ and hexanethiol (Fig. 3-10a). As **3**•PF₆ has no pyrimidine ring, only one electronic state should be observed on the molecule. Actually, there occurred no blinking in the STM images of the mixed SAM (Fig. 3-10b,c). Aggregated apparent height data of **3** were fitted with one Gaussian component with an apparent height of 1.0 nm by the least square method (Fig. 3-10d). This result proves that the blinking of **1** originates from the electrochemical potential changes, excluding the possible effect of either the structural fluctuation or the oxidation state of the Cu center.

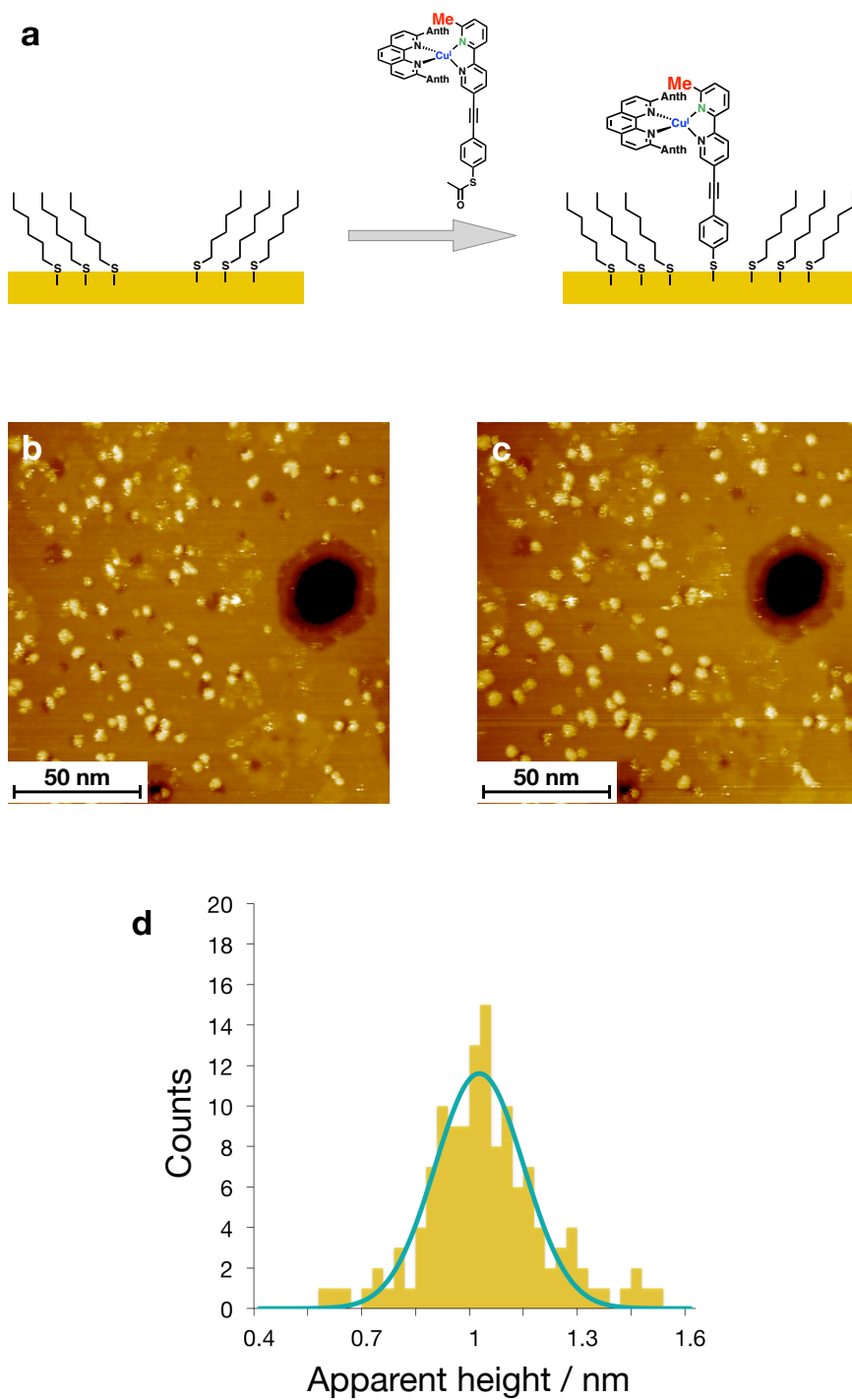


Fig. 3-10 STM observation of individual molecules **3**. (a) The mixed SAM of **3** and 1-hexanethiol used during STM. (b,c) Successive STM topographic images of the mixed SAM of **3**. $V_s = 1.1$ V, $I_t = 0.1$ nA. (d) Apparent height counts of **3**.

3-3-5 STM observation under UHV condition at 68 K

The blinking behavior was also observed in the STM measurement conducted with the mixed SAM of **1** and 1-hexanethiol under UHV condition at 68 K (Fig. 3-11). The rough estimation from Eyring plot of complex gave the small value for the rate constants at 68 K. Although the rotation is not likely to occur at this temperature from macroscopic level of cyclic voltammetry, it actually occurred at the microscopic level with the long time interval between the two states, indicating that the rotation was thermally suppressed at low temperature.

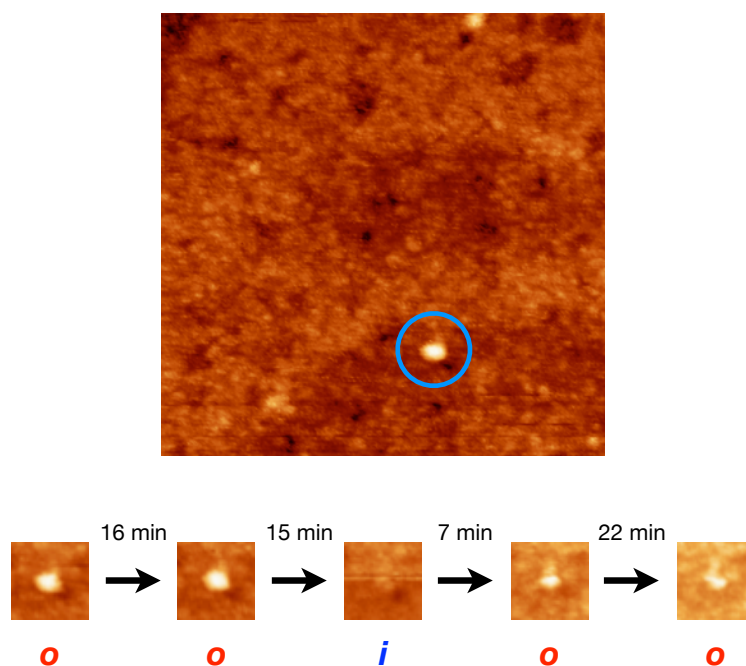


Figure 3-11 STM observation of the mixed SAM of **1** and 1-hexanethiol under UHV at 68 K. Scale: 50 nm \times 50 nm.

3-4 Conclusion

The Cu-pyrimidine complex **1** was inserted into the matrix of 1-hexanethiols on the Au surface to facilitate tracking individual molecules for an hour. The successive STM images indicate that the molecules randomly switched between two conductivity states during the measurement. The two kinds of states originated from the two rotational isomers with different electron density distributions. Although the rotation of each molecule was random, the whole system was found to establish thermodynamic equilibrium as the aggregated apparent height data had the two Gaussian components with the ratio corresponding to the equilibrium ratio of the two isomers in the Cu(I) state. This conclusion is further supported by the additional Cu complex **3** that shows no conductivity changes. Since the driving force for the rotational process is thermal energy, the time interval between the two states was found to be longer at 68 K than at room temperature.

3-5 References

- (1) Baba, D., Ono, Y., Electron transport material and organic electroluminescence element using same. PCT Int. Appl. WO 2012060374 A1 (2012).
- (2) Bumm, L. A.; Arnold, J. J.; Cygan, M. T.; Dunbar, T. D.; Burgin, T. P.; Jones, L.; Allara, D. L.; Tour, J. M.; Weiss, P. S. *Science* **1996**, *271*, 1705–1707.
- (3) Tsoi, S.; Griva, I.; Trammell, S. A.; Blum, A. S.; Schnur, J. M.; Lebedev, N. *ACS Nano* **2008**, *2*, 1289–1295.
- (4) Majima, Y.; Ogawa, D.; Iwamoto, M.; Azuma, Y.; Tsurumaki, E.; Osuka, A. *J. Am. Chem. Soc* **2013**, *135*, 14159–14166.
- (5) Seo, S.; Lee, H. *J. Phys. Chem. C* **2011**, *115*, 15480–15486.
- (6) Poirier, G.; Pylant, E. *Science* **1996**, *272*, 1145–1148.
- (7) Donhauser, Z. J.; Mantooth, B. A.; Kelly, K. F.; Bumm, L. A.; Monnell, J. D.; Stapleton, J. J.; Price, D. W., Jr; Rawlett, A. M.; Allara, D. L.; Tour, J. M.; Weiss, P. S. *Science* **2001**, *292*, 2303–2307.
- (8) Ramachandran, G. K.; Hopson, T. J.; Rawlett, A. M.; Nagahara, L. A.; Primak, A.; Lindsay, S. M. *Science* **2003**, *300*, 1413–1416.
- (9) Moore, A. M.; Dameron, A. A.; Mantooth, B. A.; Smith, R. K.; Fuchs, D. J.; Ciszek, J. W.; Maya, F.; Yao, Y.; Tour, J. M.; Weiss, P. S. *J. Am. Chem. Soc.* **2006**, *128*, 1959–1967.

Chapter 4

Two-Step Rotation of a Twin Rotor

4-1 Introduction

This chapter is devoted to a description of the two-step rotational isomerization of a twin rotor, $4\cdot\text{PF}_6$, comprising a 4,4'-dimethyl-2,2'-bipyrimidine ligand (Fig. 4-1).¹ This complex has three isomers, *ii*-isomer, *io*-isomer and *oo*-isomer, according to the directions of the methyl groups, and the redox potential shift between the *ii*- and *oo*-isomer should be twice as large as that of the existing Cu-pyrimidine system. Cyclic voltammetry evidenced the three distinct redox waves and the large potential shift of $4\cdot\text{PF}_6$.

The three different redox waves were first accomplished with $4\cdot\text{PF}_6$, while two papers have already been reported for the twin rotors consisting of other ligands.^{2,3} In the first paper, mononuclear and dinuclear copper complexes were synthesized with a 4,4'-dimethyl-2,2'-bipyrimidine and bis[2-(diphenylphosphino)phenyl] ether (DPEPhos). Due to the bulky DPEPhos ligands, two rotational steps were not realized in these complexes; a mononuclear complex could have only two isomers (*ii*-isomer was not observed) and a dinuclear complex could not even show isomerization. In the second paper, three isomers were observed by ¹H-NMR; nevertheless, there was no correlation between two rotational steps as the copper complex had only two redox waves meaning that the redox potential of a Cu center in *i*-form (or *o*-form) of *io*-isomer are almost identical to that of *ii*-isomer (or *oo*-isomer). $4\cdot\text{PF}_6$ has overcome the above issues and has three distinct redox potentials.

Of particular note is that NMR experiments and cyclic voltammetry indicated the clear difference between the two rotational processes, which is discussed in terms of kinetics and thermodynamics based on simulative analysis in the following sections.

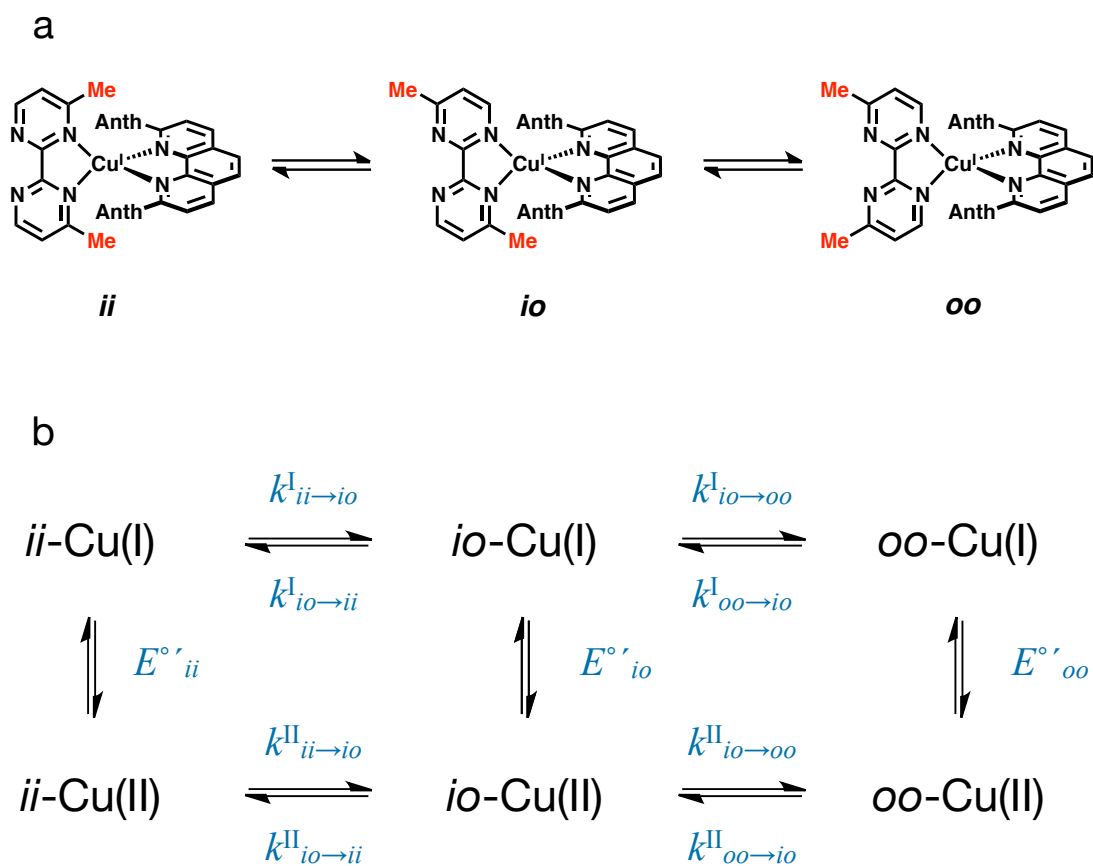


Fig. 4-1 Rotational isomerization of $4 \cdot \text{PF}_6$. (a) The three rotational isomers of $4 \cdot \text{PF}_6$. Anth = 9-anthryl. (b) Schematic of the isomerization in the Cu(I) and Cu(II) states.

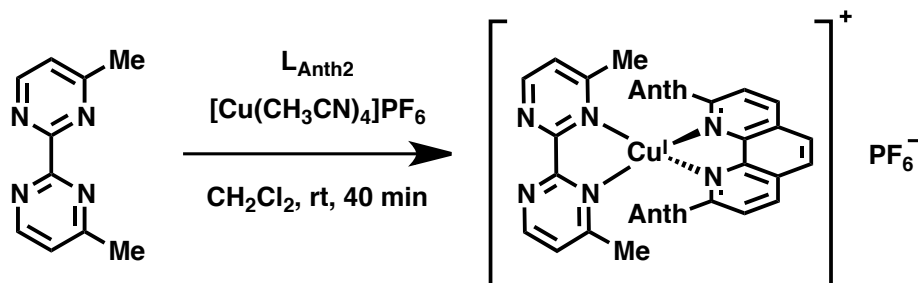
4-2 Experimental

4-2-1 Materials

Tetra-*n*-butylammonium hexafluorophosphate (purchased from Tokyo Chemical Industry) was recrystallized from HPLC-grade ethanol and dried under vacuum for 24 h. 2,9-Bis(9-anthracenyl)-1,10-phenanthroline ($L_{\text{Anth}2}$)^{4,5} and 4,4'-dimethyl-2,2'-bipyrimidine (Me_2bipym)⁶ were prepared according to literature methods. Other chemicals were used as purchased.

4-2-2 Synthesis

[Cu(Me₂bipym)(L_{Anth2})]PF₆ (4·PF₆)



2,9-bis(9-anthracenyl)-1,10-phenanthroline (L_{Anth2}, 49.1 mg, 92.2 μmol) and [Cu(CH₃CN)₄]PF₆ (34.6 mg, 94.8 μmol) were stirred for 40 min in dichloromethane (4 ml) under nitrogen atmosphere. 4,4'-dimethyl-2,2'-bipyrimidine (Me₂bipym, 20 mg, 58 μmol) was added to the resulted orange solution, and the solution immediately changed to deep red. After filtration, diethyl ether was added to the filtrate to precipitate 4·PF₆ as a deep red solid. Yield: 17 mg (20 %). ¹H NMR (500 MHz, (CD₃)₂CO, 253 K) δ 9.31 (d, *J* = 8.1 Hz, phen, *ii*), 9.27 (d, *J* = 8.1 Hz, phen, *io*), 9.25 (d, *J* = 8.1 Hz, phen, *oo*), 8.68 (s, phen, *ii*), 8.66 (s, phen, *io*), 8.64 (s, phen, *oo*), 8.54 (d, *J* = 8.1 Hz, phen, *ii*), 8.46 (d, *J* = 8.1 Hz, phen, *io*), 8.44 (d, *J* = 8.1 Hz, phen, *oo*), 8.40 (d, *J* = 4.8 Hz, bpym, *ii*), 8.28 (d, *J* = 4.9 Hz, bpym, *io*), 8.04 (s, Anth, *io*), 8.03 (s, Anth, *oo*), 8.01 (s, Anth, *ii*), 7.63-7.60 (m), 7.40 (d, *J* = 8.7 Hz, Anth), 7.37 (d, *J* = 8.7 Hz, Anth), 7.32-7.29 (m), 7.25 (d, *J* = 5.3 Hz, bpym, *io*), 7.22-7.09 (m), 6.77 (d, *J* = 4.8 Hz, bpym, *ii*), 6.66 (d, *J* = 4.9 Hz, bpym, *io*), 6.54 (d, *J* = 5.3 Hz, bpym, *io*), 6.45 (d, *J* = 5.3 Hz, bpym, *oo*), 2.41 (s, Me, *o*), 2.37 (s, Me, *io*), 1.57 (s, Me, *io*), 1.50 (s, Me, *ii*). ESI-TOF-MS *m/z* 781.2144 (calcd. for [M-PF₆]⁺, 781.2141).

4-2-3 Experimental apparatus

NMR, ESI-TOF MS

¹H NMR spectra were recorded with a Bruker DRX500 spectrometer. In VT ¹H NMR experiments, the sample tube was introduced into the machine cooled to 203 K, and the data was acquired during the heating process. ESI-TOF mass spectra were recorded using a Micromass LCT spectrometer.

Cyclic voltammetry

Cyclic voltammograms was recorded with ALS 750A electrochemical analyzers (BAS. Co., Ltd.). The working electrode was a 0.3 mm ϕ glassy carbon disc embedded in glass, a platinum wire served as the auxiliary electrode, and the reference electrode was an Ag⁺/Ag electrode (a silver wire immersed in 0.1 M Bu₄NClO₄/0.01 M AgClO₄/CH₃CN). The solutions were deoxygenated with pure argon before measurement. Cyclic voltammograms of **4**·PF₆ were simulated with the BASi Digisim 3.03a software.

4-3 Results and discussion

4-3-1 Variable-temperature ^1H NMR

Variable-temperature ^1H NMR measurements were conducted by cooling the sample solution to 203 K, and then heating it gradually. The ^1H NMR spectra of $4\cdot\text{PF}_6$ at 203 K showed three signals that were assigned to the protons at the 5-position of the *oo*-, *io*-, and *ii*-isomers (Fig. 4-2a,b), considering the shielding effect of the Cu(I) center.^{7,8} The ratios of the three isomers calculated from the integrated values of the peaks were *oo* : *io* : *ii* = 1 : 6 : 3 at 203 K. The signal splitting that emerged upon heating indicates that the interconversion rate of the isomers competed with the timescale of the NMR measurements.

Characteristic behavior was observed in the plot of the ratios of isomers versus temperatures (Fig. 4-3). Below 223 K, the ratio of the isomers was almost constant, indicating that the rotations were frozen. From 223 to 243 K, the ratio of the *oo*-isomer increased and that of the *io*-isomer decreased. The ratio of the *ii*-isomer remained constant in this region. These results suggest that only the rotation between the *oo*- and *io*-isomers occurred. Above 243 K, the rotation between *io*- and *ii*-isomers was observed, indicating two-step rotational behavior.

Simulative analysis was performed to take a close look at the change of the broadening ^1H NMR signals of the protons of the 5th position of pyrimidine rings (Fig. 4-2a). The simulated spectra and the parameters for them are shown in Fig. 4-4 and Table 4-1. The spectra at 203 K and 213 K were reproduced well by assuming that the two rotations are frozen ($k_{ii\rightarrow io}^1 = k_{io\rightarrow oo}^1 = 0$ (s^{-1})). At the temperature above 213 K, the rotation rate of *io* \rightarrow *oo*, $k_{io\rightarrow oo}^1$, became greater than 0, while $k_{ii\rightarrow io}^1$ could take 0 below 243 K, indicating the different activation temperatures as seen in Fig. 4-3.

Eyring plots in Fig. 4-5 show a significant difference in the slopes of the fitted lines of the *ii* \rightarrow *io* rotation and the *io* \rightarrow *oo* rotation; the attenuation of the *ii* \rightarrow *io* rotation rate is faster than *io* \rightarrow *oo* rotation, which is consistent with the rotation rates estimated from the simulated cyclic voltammograms discussed later (Fig. 4-10). At the lower ends of the two lines at low temperature (223 K for *io* \rightarrow *oo* rotation and 243 K for *ii* \rightarrow *io* rotation), the kinetic constants are 0.02 s^{-1} . This would be the minimum limit of rate constants for the system to reach equilibrium within a reasonable time. Therefore, it can be concluded that the difference of activation temperatures is derived from the

temperature dependence of the rate constants; the $ii \rightarrow io$ rotation freezes at higher temperature than $io \rightarrow oo$ rotation.

Note that the cooling is slow enough for the system to reach the equilibrium at the temperatures above the freezing points, as confirmed by van't Hoff plots obtained from the integrated values of ^1H NMR signals (Fig. 4-6). The plots in Fig. 4-6 can be approximated by the first order lines above the temperature where the rotation is frozen, suggesting that the system reaches the equilibrium in this temperature range, while the $\text{Ln } K^1$ value below the temperature is roughly constant due to the freezing of the rotation. the cooling is not rapid but slow enough for the system to reach the equilibrium at the temperatures above the freezing points. Therefore, the freezing of the high-temperature ratio did not occur in this experiment and the system reaches the thermodynamic equilibrium at the temperatures above the freezing points.

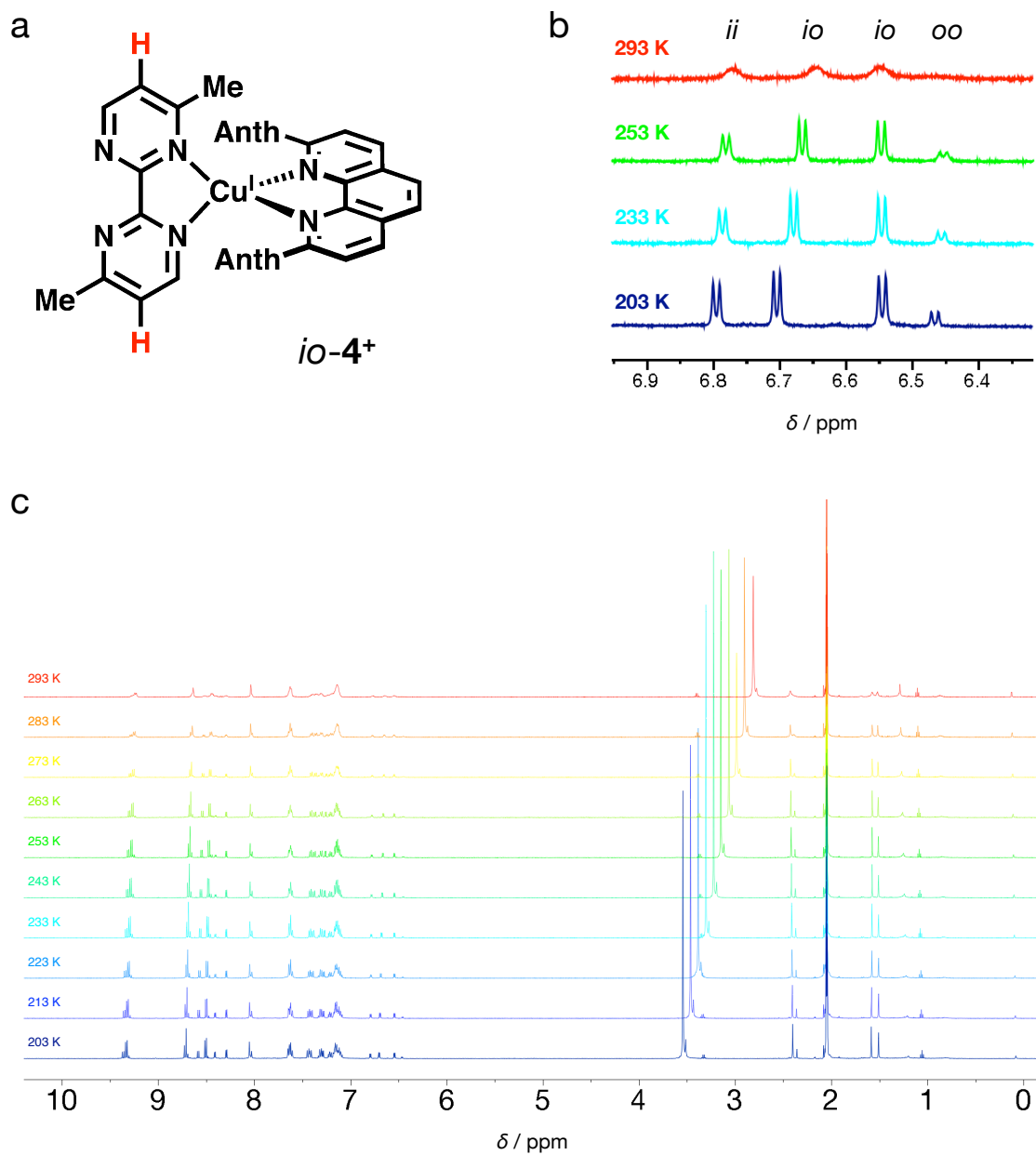


Fig. 4-2 Variable-temperature ^1H NMR measurements of $4\cdot\text{PF}_6$ in acetone- d_6 . (a) *io*-isomer of 4^+ . (b) ^1H NMR spectra of protons labeled red in (a). (c) Full scale ^1H NMR spectra.

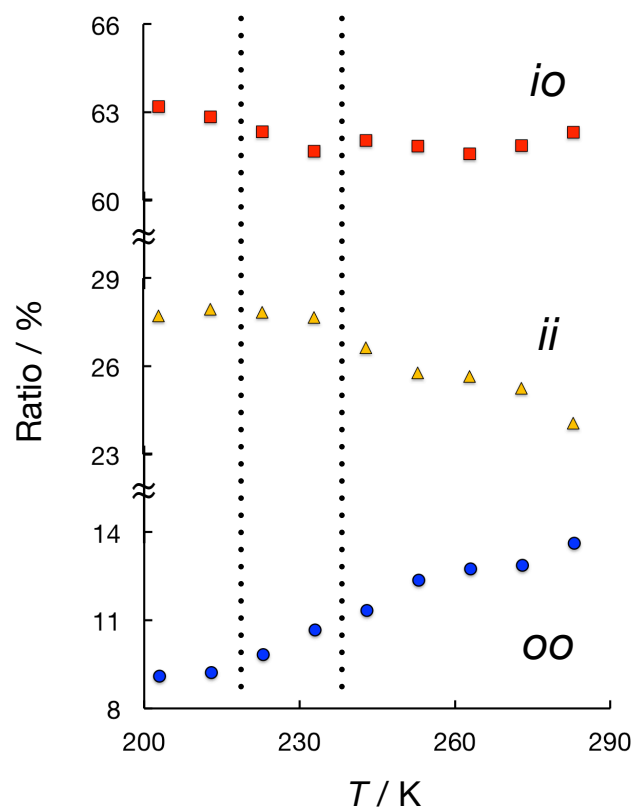


Fig. 4-3 Ratio of the isomers calculated from the integrated value of signals at different temperatures. Dotted lines indicate the temperatures at which rotation occurs.¹⁴

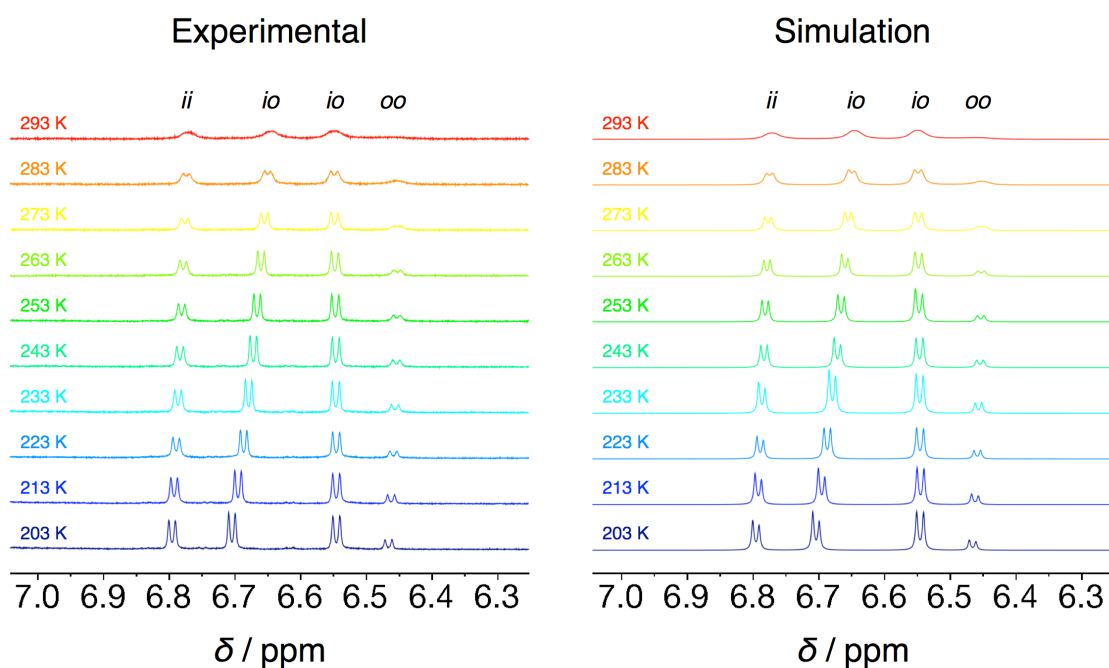


Fig. 4-4 Experimental and simulated ^1H NMR spectra of $4\cdot\text{PF}_6$ in acetone- d_6 at various temperatures.¹⁴

Table 4-1 Kinetic parameters for simulative analysis on ^1H NMR spectra

T / K	$k_{ii \rightarrow io}^1 / \text{s}^{-1}$	$k_{io \rightarrow oo}^1 / \text{s}^{-1}$
203	0	0
213	0	0
223	0	0.02
233	0	0.1
243	0.02	0.3
253	0.1	0.4
263	0.4	0.9
273	3	2
283	8.6	5.4
293	27	15

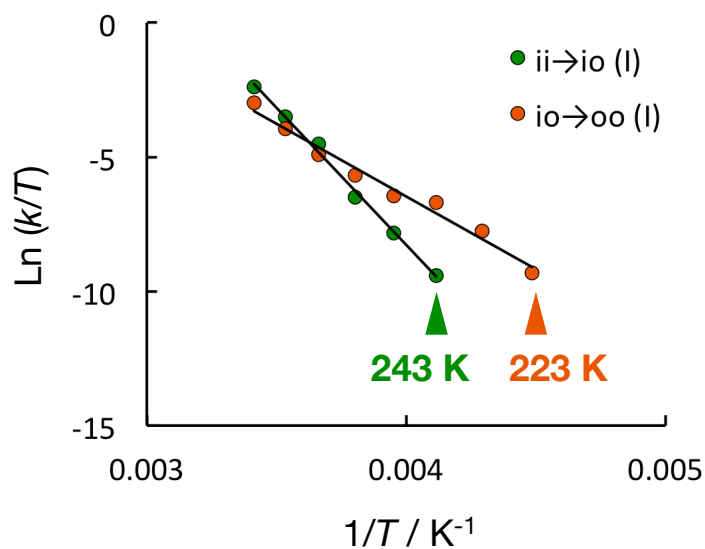


Fig. 4-5 Eyring plots of the $ii \rightarrow io$ rotation and $io \rightarrow oo$ rotation based on the rate constants estimated by simulative analysis on ^1H NMR.¹⁴

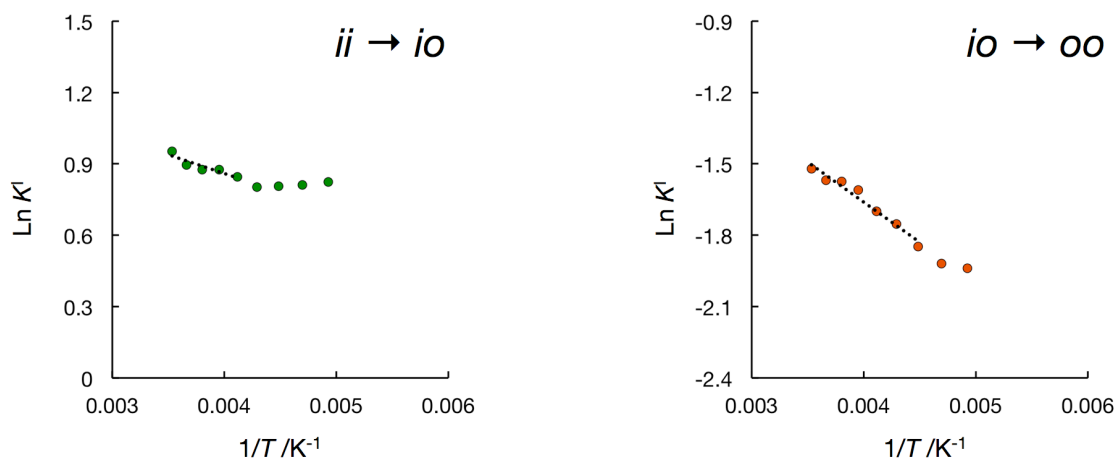


Fig. 4-6 van't Hoff plots obtained from the integrated values of the ^1H NMR signals in acetone- d_6 .¹⁴

4-3-2 Cyclic voltammetry

Cyclic voltammograms of $4\cdot\text{PF}_6$ at 293 K (Fig. 4-7a,b) show three redox signals, which were assigned to the redox reactions of the *oo*-, *io*-, and *ii*-isomers, respectively, from the negative to the positive potential, based on the electrochemistry of Cu complexes.^{9,10} The rotational behaviour was observed as the peak currents changed, particularly in the cathodic sweep. The reduction current was larger than the oxidation current for the *oo*-isomer, whereas it was smaller than the oxidation current for the *ii*- and *io*-isomers, suggesting that the *ii*- and *io*-isomers were converted to the *oo*-isomer in the Cu(II) state. This is consistent with our previous results for one pyrimidine rotation. In the Cu(II) equilibrium state, a rotor strongly prefers the outer form to the inner form because of the increase in steric hindrance owing to the conformational distortion arising from the conversion from the tetrahedral geometry of Cu(I) to the square planar geometry of Cu(II). The conversion was more obvious at the slower scan rate where the rotation took place before the reduction (Fig. 4-7b). Cyclic voltammetry at 219 K showed negligible differences between the anodic and the cathodic waves, even at a slow rate of 50 mV s^{-1} (Fig. 4-7h), indicating that rotation was frozen at 219 K within the time scale of cyclic voltammetry.

Simulative analysis was performed on the cyclic voltammograms taken at 219, 253, 273, and 293 K to obtain the kinetic and thermodynamic parameters for the rotational isomerization (Fig. 4-8). The simulated curves reproduced the voltammograms well by assuming that the two-step interconversion mechanism is dominant and the direct conversion between *oo*- and *ii*-isomers is negligible (Table 4-2). The voltammograms taken at 219 K could be simulated by assuming that rotation was frozen. The three overlapped redox waves were deconvoluted into three waves: $E^{\circ}_{oo} = 0.28\text{ V}$, $E^{\circ}_{io} = 0.48\text{ V}$, and $E^{\circ}_{ii} = 0.61\text{ V}$ vs Ag^+/Ag . By simply increasing the number of rotors, we achieved a larger potential shift for isomerization within a single molecule compared with our previous Cu complexes consisting of just one rotor. The redox potential shifts for each rotational step were different: $E^{\circ}_{io} - E^{\circ}_{oo} = 0.20\text{ V}$ and $E^{\circ}_{ii} - E^{\circ}_{io} = 0.13\text{ V}$. This means that the molecule requires different energies for each ring rotation. The rate constants were also estimated by the simulative analysis. They are described in the following section.

Note that a comparison of the rotation rate constants in the Cu(I) state ($k_{oo\rightarrow io} > k_{io\rightarrow ii}$ and $k_{ii\rightarrow io} > k_{io\rightarrow oo}$) reveals that the rate of *ii* \rightarrow *io* (or *oo* \rightarrow *io*) rotation is faster than that

of the subsequent $io \rightarrow oo$ (or $io \rightarrow ii$) rotation. This implies that $4 \cdot \mathbf{PF}_6$ shows unique behaviour, where the first ring rotation decelerates the second.

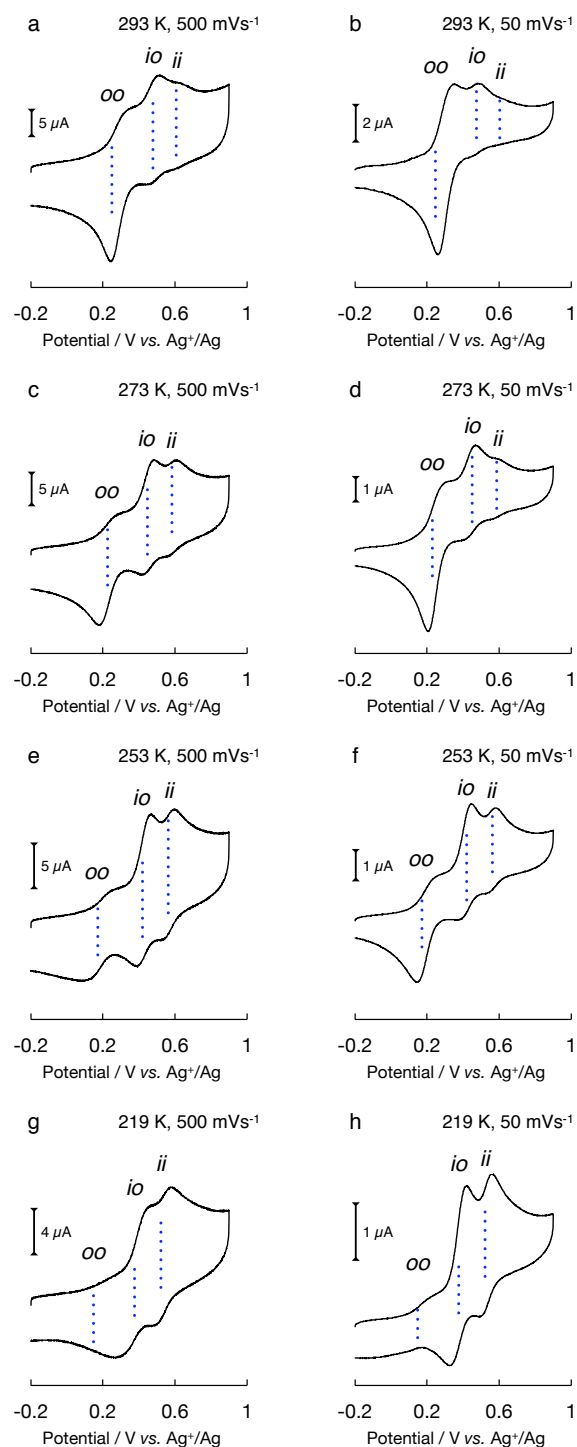


Fig. 4-7 Cyclic voltammograms of 4^+ (0.5 mM) in 0.1 M $n\text{Bu}_4\text{NPF}_6$ -acetone at various temperatures and scan rates. (a) 293 K and 500 mVs^{-1} , (b) 293 K and 50 mVs^{-1} , (c) 273 K and 500 mVs^{-1} , (d) 273 K and 50 mVs^{-1} , (e) 253 K and 500 mVs^{-1} , (f) 253 K and 50 mVs^{-1} , (g) 219 K and 500 mVs^{-1} , and (h) 219 K and 50 mVs^{-1} . All voltammograms are for the first cycle.¹⁴

Table 4-2 Fitting parameters of the ring inversion processes for $4\cdot\text{PF}_6$ in 0.1 M $n\text{Bu}_4\text{NPF}_6\text{-acetone}^{14}$

	293 K	273 K	253 K	219 K
E_{oo} / V	0.265	0.22	0.185	0.14
E_{io} / V	0.48	0.449	0.425	0.375
E_{ii} / V	0.61	0.584	0.57	0.53
$K^{\text{I}}_{ii\rightarrow io}$	2.6	2.5	2.2	2
$K^{\text{I}}_{io\rightarrow oo}$	0.2	0.18	0.17	0.14
$K^{\text{II}}_{ii\rightarrow io}$	4.5×10^2	7.7×10^2	1.3×10^3	7.3×10^3
$K^{\text{II}}_{io\rightarrow oo}$	9.9×10^2	3.1×10^3	1.1×10^4	3.6×10^4
$k^{\text{I}}_{ii\rightarrow io} / \text{s}^{-1}$	11	1.3	0.1	0
$k^{\text{I}}_{io\rightarrow oo} / \text{s}^{-1}$	8	2.7	0.5	0
$k^{\text{I}}_{oo\rightarrow io} / \text{s}^{-1}$	40	15	3	0
$k^{\text{I}}_{io\rightarrow ii} / \text{s}^{-1}$	4	0.5	0.05	0
$k^{\text{II}}_{ii\rightarrow io} / \text{s}^{-1}$	3.2	1.5	6.4×10^{-1}	0
$k^{\text{II}}_{io\rightarrow oo} / \text{s}^{-1}$	5.0	3.1	1.1	0
$k^{\text{II}}_{oo\rightarrow io} / \text{s}^{-1}$	5.0×10^{-3}	1.0×10^{-3}	1.0×10^{-4}	0
$k^{\text{II}}_{io\rightarrow ii} / \text{s}^{-1}$	7.0×10^{-3}	2.0×10^{-3}	5.0×10^{-4}	0
α_{oo}	0.5	0.5	0.3	0.5
α_{io}	0.5	0.5	0.5	0.35
α_{ii}	0.5	0.5	0.5	0.35
R_u	700	800	1000	1600
C_{dl} / F	4.2×10^{-6}	4.2×10^{-6}	4.2×10^{-6}	3.0×10^{-6}
$D / \text{cm}^2 \text{s}^{-1}$	1.2×10^{-5}	8.5×10^{-6}	4.5×10^{-6}	2.0×10^{-6}

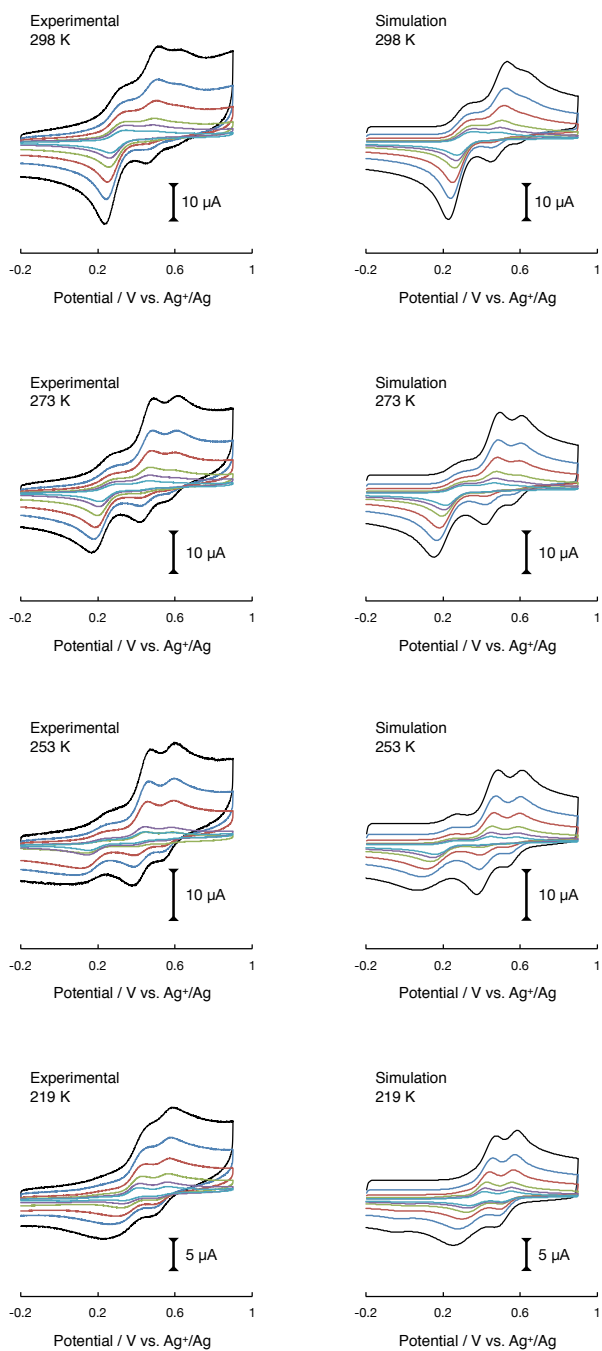


Fig. 4-8 Experimental and simulated cyclic voltammograms of 4^+ (0.5 mM) in 0.1 M $n\text{Bu}_4\text{NPF}_6$ -acetone at various temperatures and scan rates (1000, 500, 250, 100, 50, 25 mVs^{-1}). All voltammograms are for the first cycle.¹⁴

4-3-3 Kinetic and thermodynamic properties of two rotational steps

van't Hoff plots (Fig. 4-9) and Eyring plots (Fig. 4-10) gave the standard Gibbs free energies (ΔG°) and activation Gibbs free energies (ΔG^\ddagger) (Table 4-3). The free energy diagram shown in Fig. 4-11 summarizes these values. The *ii*-isomer is thermodynamically more stable than the *oo*-isomer; however, the *ii*-isomer is less stable than the *io*-isomer due to the balance of the electronic and steric effects of the methyl groups at the inner position.^{7,11} The diagram confirms that the *ii* \rightarrow *io* rotation is kinetically favoured compared with the subsequent *io* \rightarrow *oo* rotation. The deceleration of the second rotation is more obvious in the *oo*-isomer rotations; the ΔG^\ddagger value for the *oo* \rightarrow *io* rotation is substantially lower than the ΔG^\ddagger value for the subsequent *io* \rightarrow *ii* rotation.

There is good agreement between the ΔG° values obtained from cyclic voltammetry and the ratio of the isomers calculated in NMR experiments. This is because the equilibrium constants calculated from NMR experiments were first chosen as initial parameters to find the best parameters in the simulative analysis on the cyclic voltammograms. The accumulated previous researches^{8,12,13} revealed that the thermodynamic stability of this system is nearly independent of the existence of electrolyte; cyclic voltammograms could be simulated well with the similar equilibrium constants to those calculated from NMR spectra. Therefore, the ΔG° values obtained from the CV experiments are also generally consistent with the ratio of the isomers in the NMR experiments.

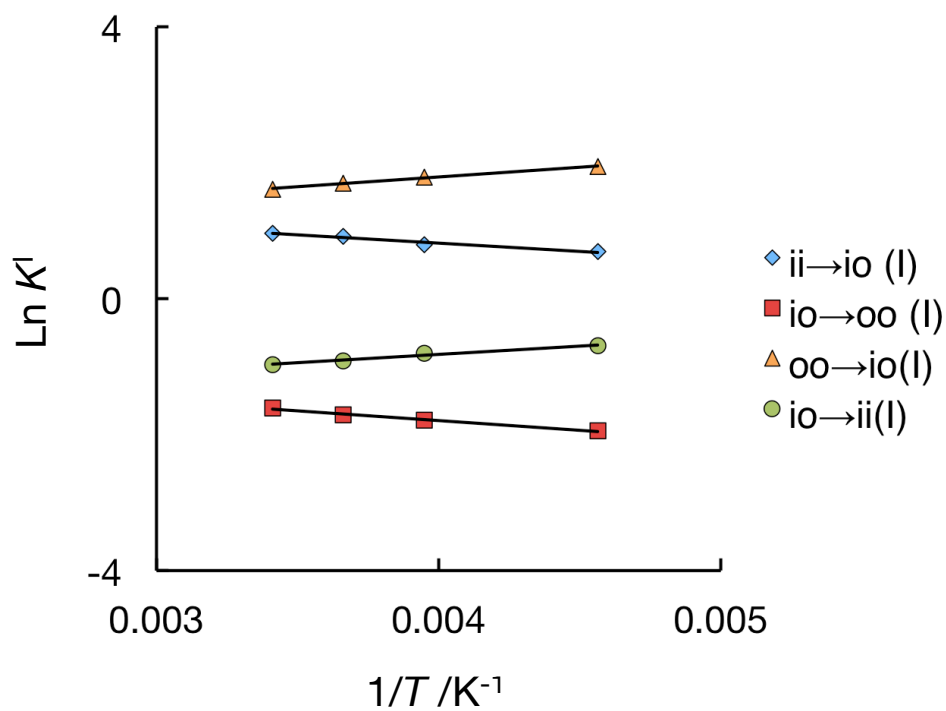


Fig. 4-9 van't Hoff plots of $4 \cdot \text{PF}_6$ in 0.1 M $n\text{Bu}_4\text{NPF}_6$ -acetone based on the simulative analysis on cyclic voltammograms.¹⁴

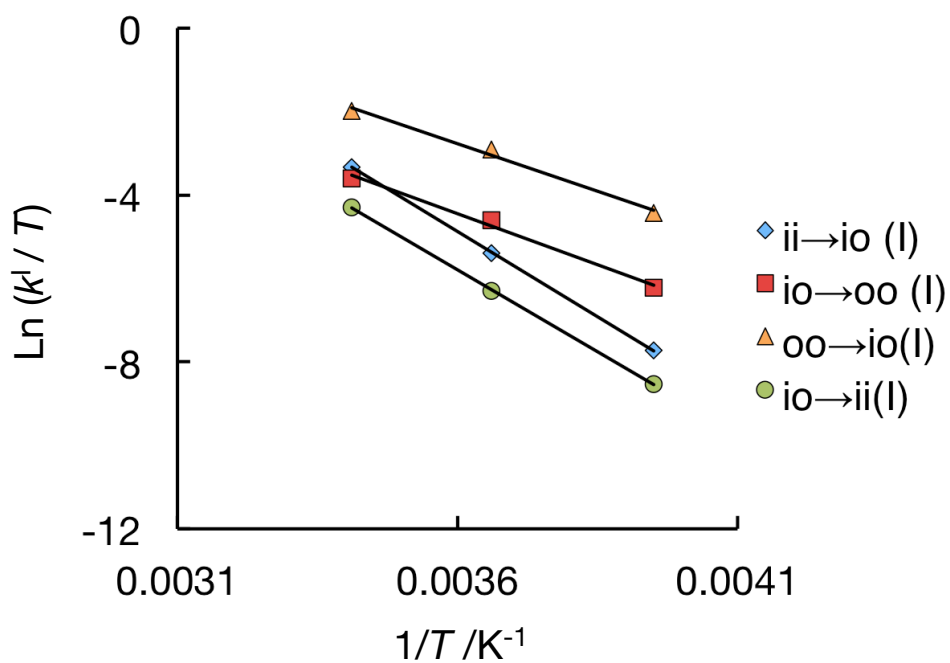


Fig. 4-10 Eyring plots of $4 \cdot \text{PF}_6$ in 0.1 M $n\text{Bu}_4\text{NPF}_6$ -acetone based on the simulative analysis on cyclic voltammograms.¹⁴

Table 4-3 Thermodynamic and kinetic parameters of $4 \cdot \text{PF}_6$ in 0.1 M ${}^n\text{Bu}_4\text{NPF}_6$ -acetone¹⁴

	$ii \rightarrow io$	$io \rightarrow oo$	$oo \rightarrow io$	$io \rightarrow ii$
$\Delta H / \text{kJ mol}^{-1}$	2.0	2.4	-2.4	-2.0
$\Delta S / \text{J K}^{-1} \text{ mol}^{-1}$	15	-5.4	5.4	-15
$\Delta G^\circ / \text{kJ mol}^{-1}$	-2.4	4.0	-4.0	2.4
$\Delta H^\ddagger / \text{kJ mol}^{-1}$	68	41	38	65
$\Delta S^\ddagger / \text{J K}^{-1} \text{ mol}^{-1}$	6.4	-88	-84	-11
$\Delta G^\ddagger / \text{kJ mol}^{-1}$	66	67	63	68

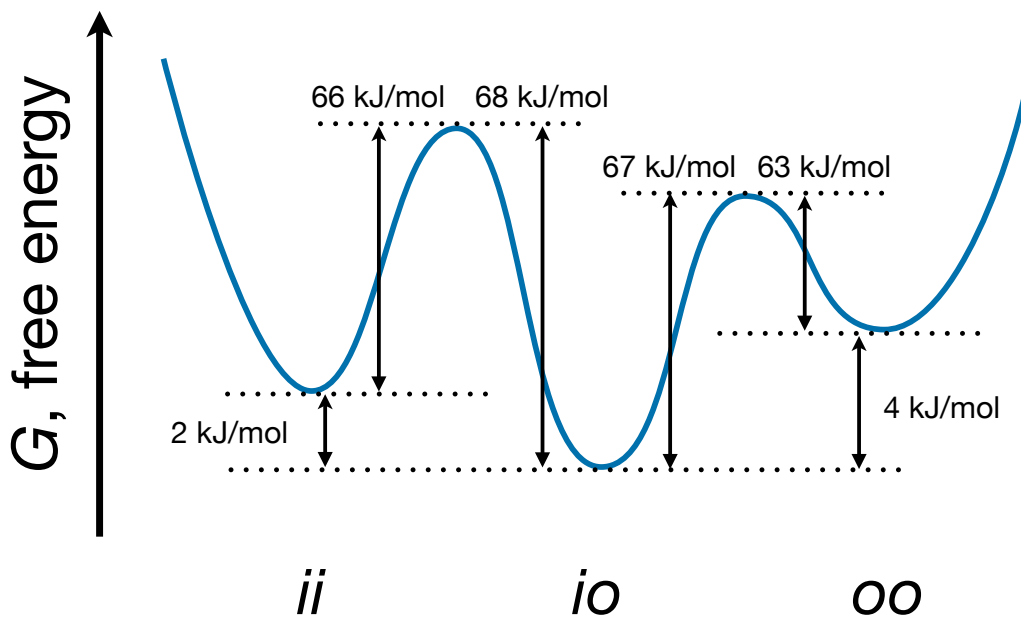


Fig. 4-11 Free energy diagram of the three isomers with the values of ΔG° and ΔG^\ddagger .¹⁴

4-4 Conclusion

The two correlated rotational motions in Cu(I) complexes were discussed in this chapter. The cyclic voltammograms of **4**·PF₆ had the three overlapping redox waves derived from the redox processes of the three isomers. The simulative analysis clarified their redox potential shifts of the two rotational processes: $E^{\circ}_{io} - E^{\circ}_{oo} = 0.20$ V and $E^{\circ}_{ii} - E^{\circ}_{io} = 0.13$ V. Therefore, increasing the number of rotors resulted in the larger redox potential shift of 0.33 V in total, which is more than double the potential shifts of 0.14 V for **1**·PF₆ (see Chapter 2).

Another important conclusion of this chapter is that the two rotational processes are activated at different temperatures, indicating the correlation of the two motions. The kinetic and thermodynamic parameters obtained from the quantitative analysis of the cyclic voltammograms also support the conclusion that first ring rotation decelerates the second rotation. This chapter first describes the three rotational isomers that exhibit distinct redox potentials and rotation rates. It was the structural differences between the isomers, caused by the correlated two rotors, that allowed these isomers distinct, contrary to our previous reports.^{2,3} In other words, the position of each methyl group differentiates the stabilities of three isomeric forms and intermediate structures, resulting in three different redox potentials and rotation rates.

4-5 References

- (1) Takara, Y.; Kusamoto, T.; Masui, T.; Nishikawa, M.; Kume, S.; Nishihara, H. A Single-Molecular Twin Rotor: Correlated Motion of Two Pyrimidine Rings Coordinated to Copper. *Chem. Commun.* **2015**, *51*, 2896–2898.
- (2) Hattori, Y.; Nishikawa, M.; Kusamoto, T.; Kume, S.; Nishihara, H. *Inorg. Chem.* **2014**, *53*, 2831–2840.
- (3) Hattori, Y.; Nishikawa, M.; Kusamoto, T.; Kume, S.; Nishihara, H. *Chem. Lett.* **2014**, *43*, 1037–1039.
- (4) Schmittel, M.; Lüning, U.; Meder, M.; Ganz, A.; Michel, C.; Herderich, M. *Heterocyclic Communications* **1997**, *3*, 493–498.
- (5) Schmittel, M.; Michel, C.; Liu, S.-X.; Schildbach, D.; Fenske, D. *European Journal of Inorganic Chemistry* **2001**, *2001*, 1155–1166.
- (6) Nasielski, J.; Standaert, A.; Nasielski-Hinkens, R. *Synthetic Communications* **1991**, *21*, 901–906.
- (7) Nomoto, K.; Kume, S.; Nishihara, H. *J. Am. Chem. Soc.* **2009**, *131*, 3830–3831.
- (8) Kume, S.; Nomoto, K.; Kusamoto, T.; Nishihara, H. *J. Am. Chem. Soc.* **2009**, *131*, 14198–14199.
- (9) Kume, S.; Kurihara, M.; Nishihara, H. *Inorg. Chem.* **2003**, *42*, 2194–2196.
- (10) Federlin, P.; Kern, J. M.; Rastegar, A.; Dietrichbuecker, C.; Marnot, P. A.; Sauvage, J. P. *New J. Chem.* **1990**, *14*, 9–12.
- (11) Kume, S.; Nishihara, H. *Dalton Trans* **2011**, *40*, 2299–2305.
- (12) Nishikawa, M.; Nomoto, K.; Kume, S.; Nishihara, H. *J. Am. Chem. Soc.* **2012**, *134*, 10543–10553.
- (13) Nishikawa, M.; Takara, Y.; Hattori, Y.; Nomoto, K.; Kusamoto, T.; Kume, S.; Nishihara, H. *Inorg. Chem.* **2013**, *52*, 8962–8970.
- (14) Figures, tables and texts are adopted from Ref. 1 by permission of The Royal Society of Chemistry.

Chapter 5

Concluding Remarks

This research aimed to develop the single-molecular system based on the Cu-pyrimidine complexes.

Chapter 2 describes the rotational isomerization of two Cu-pyrimidine complexes immobilized on the Au surfaces. Cyclic voltammetry revealed that the two isomers coexist and are interconverted, meaning that the system works not only in homogenous solution, but also in a molecularly-separated phase. The quantitative analysis of the voltammograms clarified the drastic decrease of the rotation rate on the surface compared with that in solution. This slowing effect on surface permits the isomerization to be observed by STM. The control of the rotational motion by an applied electric potential from the electrode was demonstrated in preceding electrolysis.

Single molecule study by STM is described in Chapter 3. The Cu complexes were inserted into 1-hexanethiol SAM to disperse individual molecules for continuous observation. In the successive STM images, the molecules showed random switching behavior between the two conductivity states. The accumulated data also indicated the existence of the two states, of which ratio is similar to the Cu(I) equilibrium ratio calculated by the electrochemical measurements in Chapter 2. The origin of the conductivity changes was discussed in terms of their electron density distributions of the frontier molecular orbitals obtained by DFT calculation. It was further confirmed that the conductivity change was originated from the rotational isomerization by comparison with the result of the Cu complex that did not show isomerization.

Chapter 4 presents a study to achieve tristability with the Cu-pyrimidine system. A Cu complex was synthesized with a ligand tethered with two rotors and it showed three redox waves derived from two rotational steps in cyclic voltammetry. The simulative analysis on the cyclic voltammograms clarified the different potential shift for each rotational step, suggesting that they are not equivalent. Variable temperature ^1H NMR experiments indicated two-step activation of the rotations upon heating from the rotation-frozen temperature. The difference between the two rotational steps was described in terms of the kinetic and thermodynamic parameters.

The rotational isomerization of the Cu-pyrimidine complex was visualized at the single molecule level. This research revealed that even a small degree of molecular motion can be identified by STM, if the electronic state differs with the structural changes. Miniaturization and high operating temperature are two basic requirements to fulfill for practical molecular devices. Therefore, this study would open up a new

strategy to design small molecules whose motions are accessible at room temperature, which would lead to a further development of molecular devices.

Publication

Takara, Y.; Kusamoto, T.; Masui, T.; Nishikawa, M.; Kume, S.; Nishihara, H. A Single-Molecular Twin Rotor: Correlated Motion of Two Pyrimidine Rings Coordinated to Copper. *Chem. Commun.* **2015**, *51*, 2896–2898.

Acknowledgement

This work was established under a lot of supports of many persons, and I would like to express my gratitude to them.

This study was fully supervised by Professor Dr. Hiroshi Nishihara (The University of Tokyo). He has always been a great help for me since I joined his laboratory in 2009. I am most grateful to him for his valuable guidance, discussion and encouragement.

I would like to express my deep gratitude to Associate Professor Dr. Shoko Kume (Hiroshima University) and Assistant Professor Dr. Tetsuro Kusamoto (The University of Tokyo) for their valuable discussions and teaching.

I am grateful to Associate Professor Dr. Yoshinori Yamanoi (The University of Tokyo), Assistant Professor Dr. Ryota Sakamoto (The University of Tokyo) and Assistant Professor Dr. Mariko Miyachi (The University of Tokyo) for their helpful comments and suggestions.

I would like to deeply acknowledge to Professor Dr. Yutaka Majima (Tokyo Institute of Technology), Assistant Professor Dr. Yasuo Azuma (Tokyo Institute of Technology) and Mr. Chun Ouyang (Tokyo Institute of Technology) for LT-UHV STM measurement.

I am thankful to my lab colleagues, Mr. Tatsuya Masui, Dr. Hiroaki Maeda, Dr. Wu Kuo-Hui and all the other members in Nishihara Laboratory for their helpful discussions and supports.

Finally, I express my sincere gratitude to my family for giving me the opportunity to study.